Acta Materialia 238 (2022) 118180

Contents lists available at ScienceDirect

Acta Materialia

journal homepage: www.elsevier.com/locate/actamat

Full length article

# Microstructure, grain boundary evolution and anisotropic Fe segregation in (0001) textured Ti thin films

Vivek Devulapalli[a,*], Marcus Hans[b], Prithiv T. Sukumar[a], Jochen M. Schneider[b], Gerhard Dehm[a], C.H. Liebscher[a]

[a] Max-Planck-Institut für Eisenforschung GmbH, Max-Planck-Straße 1, Düsseldorf 40237, Germany
[b] Materials Chemistry, RWTH Aachen University, Kopernikusstr. 10, Aachen D-52074, Germany

ARTICLE INFO

*Article history:*
Received 5 November 2021
Revised 10 July 2022
Accepted 14 July 2022
Available online 22 July 2022

*Keywords:*
Titanium
Thin films
Coincident site lattice (CSL)
Faceting
Grain boundary segregation

ABSTRACT

The structure and chemistry of grain boundaries (GBs) are crucial in determining polycrystalline materials' properties. Faceting and solute segregation to minimize the GB energy is a commonly observed phenomenon. In this paper, a deposition process to obtain pure tilt GBs in titanium (Ti) thin films is presented. By increasing the power density, a transition from polycrystalline film growth to a maze bicrystalline Ti film on $SrTiO_3$ (001) substrate is triggered. All the GBs in the bicrystalline thin film are characterized to be $\Sigma 13$ [0001] coincident site lattice (CSL) boundaries. The GB planes are seen to distinctly facet into symmetric $\{\bar{7}520\}$ and $\{13\bar{4}0\}$ and asymmetric $\{10\bar{1}0\}$ // $\{11\bar{2}0\}$ segments of 20–50 nm length. Additionally, EDS reveals preferential segregation of iron (Fe) in every symmetric $\{\bar{7}520\}$ segment. Both the faceting and the segregation are explained by a difference in the CSL density between the facet planes. Furthermore, in the GB plane containing Fe segregation, atom probe tomography is used to experimentally determine the GB excess solute to be 1.25 atoms/nm$^2$. In summary, the study reveals for the first time a methodology to obtain bicrystalline Ti thin films with strong faceting and an anisotropy in Fe segregation behaviour within the neighbouring GB facets.



## 1. Introduction

Titanium (Ti) and its alloys have a high strength-to-weight ratio, excellent corrosion resistance and biocompatibility [1]. These properties make it an attractive structural material, mainly in the aerospace and biomedical industries [2]. Despite possessing the majority of the desired properties for automotive industries, the most significant impediment to Ti alloys' widespread use has been their high cost. Many alloying additions have been investigated in recent decades to not only improve mechanical and high-temperature properties but also to make them affordable [3,4].

Ti exhibits an allotropic transition from the low-temperature hexagonal close-packed (hcp) $\alpha$-phase to the high-temperature body-centered cubic (bcc) $\beta$-phase at 882°C. The alloying elements added to Ti are classified as $\alpha$-stabilizers (Al, Sn, Ga, Zr, C, O, and N), $\beta$-stabilizers (Fe, V, Mo, Nb, Ta, and Cr), or neutral elements (Zr, Sn, and Si), based on the phase they stabilize. Iron (Fe) is one of the most cost-effective $\beta$ stabilizing alloying elements and has therefore attracted plentiful attention [5–8]. The addition of Fe can result in its segregation at grain boundaries (GBs), $\beta$-phase formation, or precipitation of intermetallic compounds. Ti-Fe alloys are either $\beta$-phase or a mixture of $\alpha$- and $\beta$-phase, where the phase-fraction depends on the alloy composition [9]. When added in excess of 2.5 at.%, Fe is known to form $\beta$-flakes at the GBs which are deleterious to the material properties [10]. Additionally, two metastable phases, $\alpha'$-Ti (hcp), and $\omega$-Ti(Fe), have been observed during martensitic transformation of Ti-Fe alloys [11–15]. The $\omega$-Ti(Fe) is a high-pressure Ti phase which is retained at low pressure in Ti-Fe alloys. However, the role of Fe in the $\alpha \rightarrow \beta$ and in $\beta \rightarrow \omega$ phase transition is not clear yet [16].

A change in the chemical composition of the interfacial region changes the thermodynamic driving force for solid-state phase transition [17]. Fe segregation at GBs in Ti alloys can also lead to the formation of TiFe or $Ti_2Fe$ intermetallic compounds [18].

* Corresponding author.
*E-mail addresses:* v.devulapalli@mpie.de (V. Devulapalli), hans@mch.rwth-aachen.de (M. Hans), prithiv@mpie.de (P.T. Sukumar), schneider@mch.rwth-aachen.de (J.M. Schneider), dehm@mpie.de (G. Dehm), liebscher@mpie.de (C.H. Liebscher).

https://doi.org/10.1016/j.actamat.2022.118180

These binary intermetallics have been considered as a potential choice for solid-state hydrogen storage applications [19]. Likewise, Ti-Fe alloys have also been extensively used to fabricate near-net shape parts using the blended elemental powder metallurgy (BEPM) route to achieve cost reduction [20,21]. Overall, a multitude of phase transitions have been realized in Ti-Fe alloys, but numerous questions on how Fe influences these phase transformations remain unanswered. Some of the answers are likely to lie in the GB segregation of Fe that leads to precipitation or other phase transitions.

In the case of $\alpha$-Ti, the maximum solubility of Fe is less than 0.05 at.% [22,23]. Consequently, when added in excess of solubility limit, Fe must either form secondary phases or segregate at the GBs. Although extensive studies have been performed on GB segregation in many fcc and bcc metals and alloys, limited reports have discussed GB segregation in Ti or other hcp metals. Oxygen and Carbon have been shown to weakly segregate at the Ti GBs although oxygen has a high solubility in $\alpha$-Ti [24,25]. In $\beta$-Ti, Fe and Cr have been shown to segregate at the GBs and act as grain refiners when cooling [26]. The segregation of Fe at Ti GBs has repeatedly been suggested to be responsible for pinning the GBs, leading to remarkably stable nanocrystalline Ti [25,27]. Recently, density functional theory (DFT) calculations also confirmed the presence of a high driving force for Fe to segregate at $\alpha$-Ti GB [25]. However, it is unclear how Fe pins the GBs and whether or not secondary phases contribute to this. In many cubic materials, segregation is observed to strongly vary based on the nature of the GB [28]. Nevertheless, no anisotropy in segregation with respect to the GB type in Ti or other hcp metals has ever been reported either experimentally or theoretically.

Such a systematic study of the influence of GB character on material properties requires a template-based approach to obtain desired GBs. For many metals, bicrystalline samples with predefined GB parameters have been grown using the vertical Bridgman technique for specific GB property studies [29]. However, in Ti, the hcp-bcc allotropic transition makes it impossible to fabricate bicrystals to form a specific GB. Therefore, a novel thin film deposition route to obtain bicrystalline Ti has been established here. A bicrystalline thin film here is referred to as a film that only contains a certain misorientation of the crystals, although multiple grains can be present in the same film. Such thin films with multiple grains but only two orientations of them being present have been consistently classified as bicrystalline in literature, mostly reported in cubic metals like Al on Si(100) substrate and Au on Ge(001) substrate [30–37]. To deposit such films, a thorough understanding of the impact of various deposition parameters on the microstructure of the film is required. In physical vapour deposition, the degree of ionisation of the plasma particles determines the ion flux towards the growing film [38,39]. A high ion fraction in a discharge is achieved by promoting the electron impact ionization which is achieved by using plasma of high electron density and higher temperature. Such a plasma is formed by using a pulsing unit at the target. Textured Ti films with (0002) out-of-plane orientation were recently reported using a similar deposition route [40].

In the following sections, firstly a template-based approach to obtain $\Sigma$13 GBs in thin films of Ti on $SrTiO_3$ substrate is established. Pulsed magnetron sputtering using a commercially pure Ti target with trace Fe impurities is used to obtain a bicrystalline thin film with columnar grains. Subsequently, electron backscatter diffraction (EBSD) in a scanning electron microscope (SEM) is used to characterize the thin film microstructure. The GBs contained in the thin film are analyzed in detail using a scanning transmission electron microscope (STEM) and are observed to be faceted into symmetric and asymmetric segments. Using high resolution energy dispersive spectroscopy (EDS) analysis, the segregation of Fe to these topographically complex GBs is explored.

## 2. Experiment details

### 2.1. Thin film deposition

Thin films of Ti were deposited onto 10 × 10 $mm^2$ $SrTiO_3$ (001) substrates (Crystal GmbH, Germany) using pulsed magnetron sputtering in a commercial deposition system (Ceme Con AG CC 800-9). A rectangular 500 × 88 × 10 $mm^3$ Ti target of above 99 wt.% nominal purity (grade 2) with 0.2 wt.% Fe (0.17 at.%), 0.18 wt.% O (0.54 at.%) and 0.1 wt.% C (0.54 at.%) as a major impurity was positioned at a distance of 10 cm to the substrate holder. The base pressure was 2.2 × $10^{-6}$ mbar and increased to 3 × $10^{-6}$ mbar after heating the substrate to 600 °C using radiation heaters. During deposition, an Ar flow rate was set to 200 sccm leading to a working pressure of approximately 3.8 × $10^{-4}$ mbar. A Melec SIPP2000USB-16-500-5 power supply was used and the substrates were at floating potential. Four different deposition conditions are discussed in the following article. The first film was deposited using direct current magnetron sputtering (dcMS) with 250 W power for 2.5 h where a deposition rate of 1.33 Å/s was obtained. The pulsing unit was not used in this deposition. For the subsequent three films, pulsed magnetron sputtering was used. In pulsed magnetron sputtering, the conventional sputtering source is used in a pulsing mode with a predetermined pulse duration ranging from 1 µs to 1 s to increase the current density. This additional degree of freedom to adjust the pulse duration can be used to tailor desired microstructures [41,42]. The target voltage and current variation during a single pulse is shown in Fig. 1. The time average power was set to 1500 W with a pulse duration of $t_{on}/t_{off}$ of 200/1800 µs. This led to the peak current ($I_{ion}$) of 40 A resulting in a dense film and a peak target power density of 46 W $cm^{-2}$. The three films were grown under identical conditions by keeping all the film deposition parameters unchanged but changing the post-deposition annealing duration between 2 h, 4 h and 8 h at 600 °C to investigate its influence on the film microstructure, texture and grain size. The substrate holder temperature was constantly monitored using thermocouple to measure any local changes in substrate temperature. The annealing was performed immediately post turning off the plasma without breaking the vacuum because Ti is known to be highly prone to oxidation. With a deposition rate of about 8.3 Å/s, a film thickness of 1.5 µm was obtained in ∼30 min. The venting temperature was always <70° to reduce surface oxidation [43].

### 2.2. Microstructural characterization

The preliminary investigation was carried out using a light optical microscope (LOM) to check for any cracks/ defects on the surface. Subsequently, orientation of all grains was mapped using EBSD in an SEM. An in-plane lift-out technique in a dual-beam focused ion beam (FIB) instrument (Thermo Fisher Scientific Scios 2 HiVac) with $Ga^+$-ion source was used to extract a transmission electron microscopy (TEM) lamella. The beam current was gradually reduced in several steps starting from 1 nA at 30 kV for coarse milling to eventually 27 pA at 2 kV for final polishing to obtain a thickness of <100 nm. A retractable FEI STEM 3+ detector was used in the Scios 2 HiVac dual-beam FIB/SEM at 30 kV for STEM imaging requiring lower resolution. For high-resolution STEM, a probe corrected STEM, Titan Themis 80–300 (Thermo Fischer Scientific), was used at an acceleration voltage of 300 kV. A semi-convergence angle of 23.8 mrad was used for imaging. With a camera length of 100 mm, collection angles of 78–200 mrad and 38–77 mrad were obtained for the high-angle annular dark field (HAADF) and the annular dark field (ADF) detectors, respectively. Thermo Scientific ChemiSTEM Technology using four in-column Super-X detectors was used with a beam current of ∼50 pA for the EDS anal-

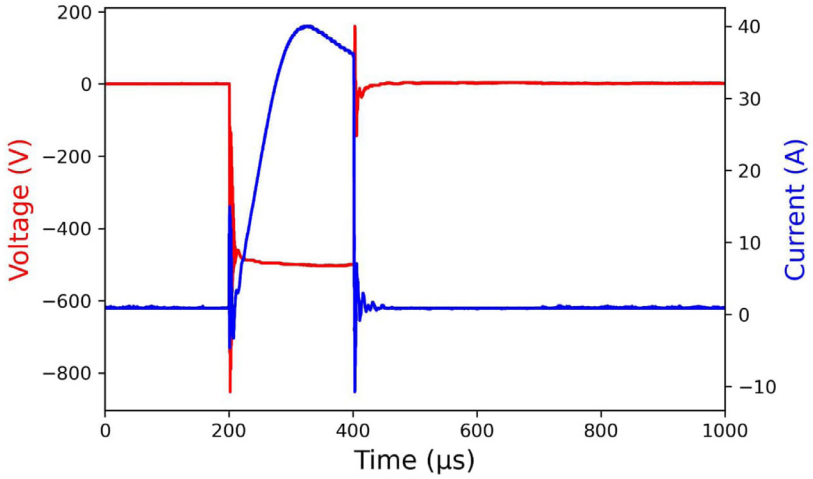


**Fig. 1.** Evolution of the target voltage and current during a single cycle of pulsed magnetron sputtering. A strong voltage overshoot is observed during ignition followed by a steady state of voltage for 200 μs resulting in a peak target power of 20 kW and peak target power density of 46 W $cm^{-2}$. The pulse period was 2 ms.

ysis. Laser-pulsed atom probe tomography (APT) was performed in a LEAP$^{TM}$ 5108XR (CAMECA) at a repetition rate of 200 kHz, a specimen temperature of about 50 K, a pressure lower than $1 \times 10^{-10}$ Torr ($1.33 \times 10^{-8}$ Pa) and a laser pulse energy of 20 pJ. The evaporation rate of the specimen was 5 atoms per 1000 pulses. Datasets were reconstructed and analyzed with the AP Suite 6.1 software based on the voltage curves.

Using the results from APT, the interfacial excess was experimentally determined by selecting a region of interest (ROI) across the interface where the solute is segregated and plotting the so-called, *ladder diagram*. A *ladder diagram* is established by taking the total number of atoms in the ordinate and the integral of solute atoms in the abscissa. A linear fit within the concentration profile of the two grains can be extrapolated to the Gibbs dividing surface (GB surface) to find the solute content in both the grains, $N_a$ and $N_b$. Using this, the Gibbsian interfacial excess is calculated as:

$$\Gamma_{excess} = \frac{N_b - N_a}{(Detection\ efficiency \times Area\ of\ ROI)} \quad (1)$$

Additional details are described in [44]. The detection efficiency was 0.52.

## 3. Results and Interpretation

### 3.1. Evolution of thin film microstructure and grain boundaries

The Ti film deposited on $SrTiO_3$ (001) at 600 °C using dcMS is characterized by SEM and EBSD as shown in Fig. 2. Following the deposition, the film was post-annealed at 600 °C for 2 h in the deposition chamber. The secondary electron (SE) image in Fig. 2 a) reveals a rough surface and small grains. Figure 2 b) shows the crystallographic orientation map based on the [0001] inverse pole figure (IPF) obtained using EBSD. The grain size is measured to be ~500 nm using the line intercept method [45]. To visualize the change in misorientations, a black line is highlighted inside the orientation map in Fig. 2b). The misorientation between every point on the line and the first point (origin) on the line is displayed as a misorientation profile chart. In the profile, a range of varying orientations is observed in Fig. 2c). Using the [$10\bar{1}0$] pole figure in Fig. 2d), two dominant textures are observed. First, a strong ($10\bar{1}1$) fiber texture is seen revealing the presence of all possible in-plane rotations. These grains are highlighted in purple in both the orientation map and the pole figure. Second, a (0002) texture is observed with only two in-plane grain rotations, with each orientation highlighted in red and blue in the pole figure. The pole figure comprises a single point per grain that is weighted by grain size; thus, the distribution of both orientations can be seen to be approximately equal. It is known that the (0002) plane has the lowest surface energy in Ti due to the highest atomic density and ($10\bar{1}1$) has the least strain energy due to the lowest elastic modulus [46]. Hence, the two orientations seem to compete and both are observed by EBSD in the film deposited by dcMS.

To understand the influence of higher ionization of the plasma and increased adatom mobility on the film microstructure, pulsed magnetron sputtering was subsequently used to deposit three additional films of Ti. The depositions were performed at 600 °C and post-annealed at the same temperature for 2 h, 4 h and 8 h. Owing to the unique microstructure of the films, the grain sizes in these films are discussed separately in the next section. For the film annealed for 4 h, a much smoother surface is obtained, as seen in Fig. 3. In Fig. 3b), the orientation map obtained from EBSD confirms that almost all of the grains have a [0001] surface plane normal. The pole figure shown in the inset is obtained from the same data set. It confirms the 30° misorientation corresponding to Σ13 [0001] GBs. The misorientation of the grains is determined from electron backscatter diffraction patterns. The position of the Kikuchi bands and hence the crystal orientation is determined by a 2D Hough transformation. It has been demonstrated that the angular resolution is <1° [47] and hence the measured grain misorientation is expected to be within this range. The exact Σ13 misorientation around the [0001] tilt axis is 28.8°. The Brandon criterion determines the amount of deviation ($\delta\theta$) from a misorientation that may be tolerated by addition of secondary dislocations/defects at the GB while maintaining a particular CSL value [48]: $\delta\theta = 15^{\circ} \times \Sigma^{-1/2}$. For a Σ13 GB one obtains $\delta\theta = 4.16$. Therefore, it can be concluded that the GBs in the present film fall within the accepted deviation of a Σ13 CSL GB. For better statistics, we show a large scan area of 40×50 μm with a step size of 70 nm in Fig. S1 which illustrates that the majority of GBs are of Σ13 type all over the film.

Furthermore, as previously observed, all of the grains with (0002) surface plane normal have either of the two orientations shown in the pole figure, which are denoted by red and blue. A purple dashed-circle is drawn in the inset of Fig. 3b) that marks the additional reflections at ~ 25° away from the center. As every reflection in the pole figure is weighted by the grain size, these additional reflections correspond to small grains of other orientations. They account for less than 2 area % of the total scan area. As a result, we follow the definition used in the literature to term

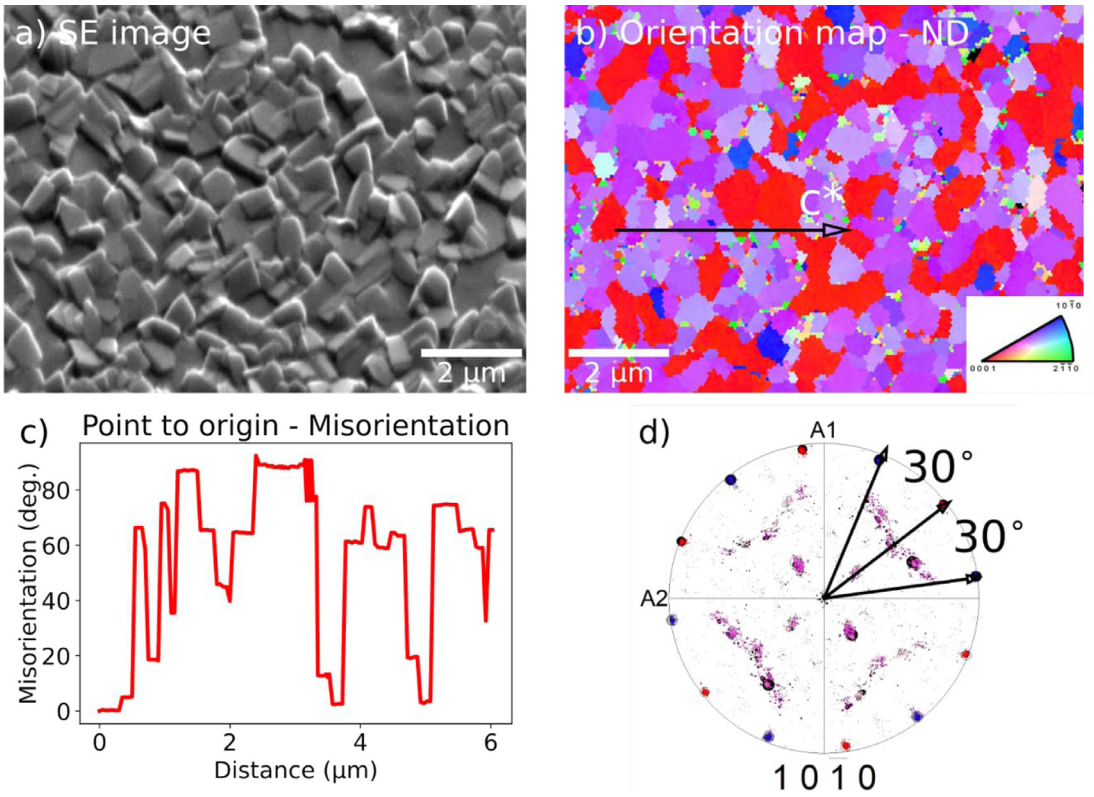


**Fig. 2.** Ti film deposited using dcMS with 250 W power on $SrTiO_3$ at 600 °C and post-annealed at 600 °C for 2 h. a) SE image showing rough surface and small grain size. b) Inverse pole figure (IPF) map obtained from electron backscatter diffraction (EBSD) revealing the two dominant surface plane orientations to be $\{10\bar{1}1\}$ and (0002). The arrow highlights the points along which a point-to-origin misorientation profile chart is plotted in (c). d) Pole figure confirming the dominance of two surface plane orientations with a fiber texture of $\{10\bar{1}1\}$ planes and only two in-plane rotations of (0002) planes.

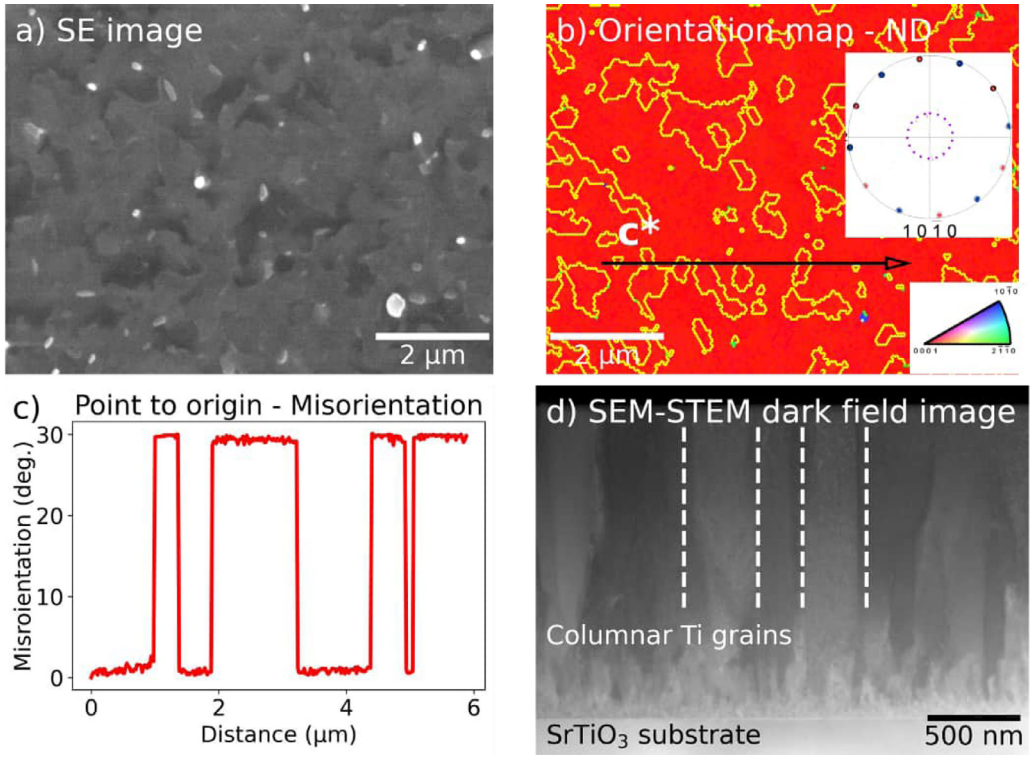


**Fig. 3.** a) SE image of Ti film deposited on $SrTiO_3$ at 600 °C using pulsed magnetron sputtering with a pulse duration of 200 µs and 1500 W power followed by post-annealed at 600 °C for 4 h showing smoother surface and relatively larger grain size. b) Inverse pole figure (IPF) map obtained from EBSD with Σ13 grain boundaries highlighted in yellow. The arrow highlights the points along which a point-to-origin misorientation profile chart is plotted in (c). The inset shows the $10\bar{1}0$ pole figure highlighting the two major orientations in blue and red, respectively. The dashed purple circle in the pole figure indicates the presence of trace $10\bar{1}0$ orientated grains. d) A dark field SEM-STEM image of the cross-section of the film reveals columnar grain growth. (For interpretation of the references to color in this figure legend, the reader is referred to the web version of this article.)

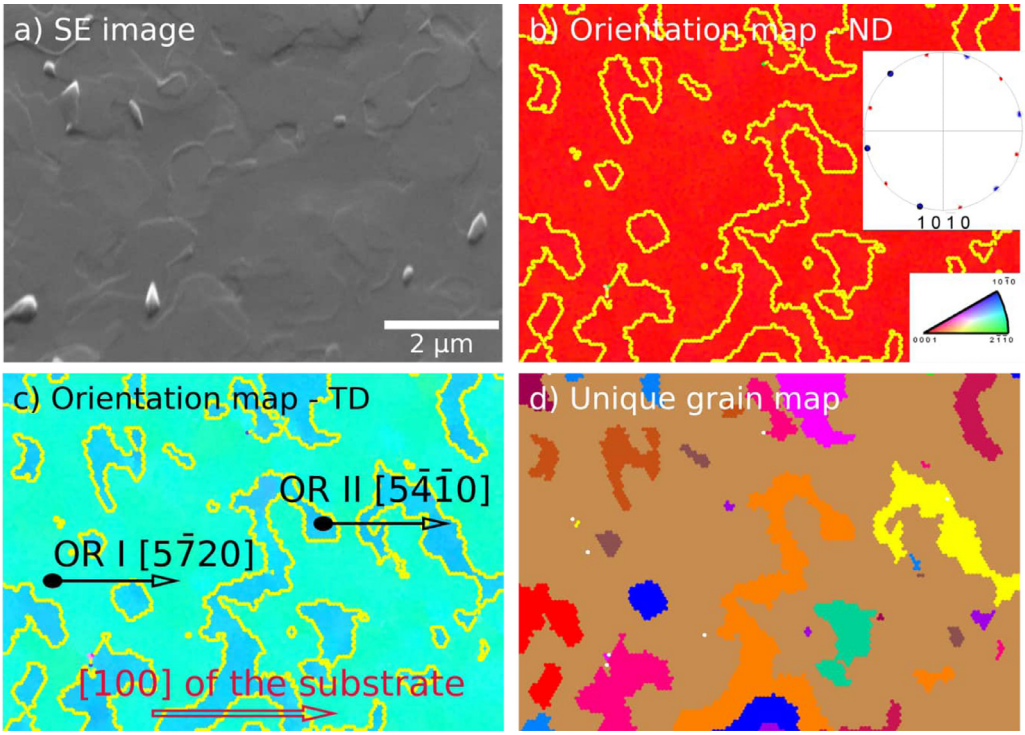


**Fig. 4.** Ti deposited on $SrTiO_3$ at 600 °C and post-annealed at 600 °C for 8 h a) SE image showing traces of grain boundaries. b) Inverse pole figure (IPF) map in the normal direction (ND) showing all grains in (0002) out of plane orientation. The inset shows the pole figure obtained from IPF confirming the ~ 30° misorientation. c) IPF map in the transverse direction (TD) with Σ13 grain boundaries highlighted in yellow. The two arrow marks in OR I and OR II grains indicate the the crystal directions parallel to [100] of the substrate. d) Unique grain map confirms that OR I is a single grain that is spread all over the substrate. All the other grains belong to OR II. All subfigures share the same scale bar as (a). (For interpretation of the references to color in this figure legend, the reader is referred to the web version of this article.)

these films as bicrystalline. This is supported by the presence of only two alternating orientations in a representative misorientation profile chart in Fig. 3c). The high peak current of 40 A during pulsed magnetron sputtering in contrast to 5 A during dcMS is responsible for the shift of surface plane orientation from (10$\bar{1}$1) and (0002) in the dcMS film to all the grains being only (0002) oriented in the pulsed magnetron sputtered film. A cross-section FIB lamella was prepared to resolve the microstructure of the film in growth direction. The majority of the grains were found to be columnar as seen in Fig. 3d). Additionally, many nanocrystalline grains are observed at the film-substrate interface. Further details of this interfacial layer are discussed in the following section where a similar distribution of fine columnar grains at the interface is observed for the film annealed for 8 h at 600 °C.

When the post annealing time is extended to 8 h, the film surface remains smooth, as seen in Fig. 4.

EBSD measurements also show the same mazed bicrystalline microstructure as observed previously. When comparing the films annealed for 4 h and 8 h, the isolated grains of other orientations are seemingly overgrown by the larger grains having (0002) orientation in the 8 h sample. The pole figure in Fig. 4b) shows the presence of only (0002) out-of-plane orientations. The full width at half maximum (FWHM) for the poles of both the grains in the pole figure is less than 1°. After 8 h of annealing, no other trace orientations are observed and all the GBs are identified to be of Σ13 type, following the Brandon criterion. Additionally, SADPs acquired from three different TEM-lamellae prepared from the same film revealed bicrystalline diffraction patterns as seen in Fig. S2.

Furthermore, by keeping the substrate's [100] direction parallel to the scan direction, we were able to determine the orientation relationship between the film and the substrate. All the grains can be primarily attributed to only two orientations. One grain is continuous and extends all over the substrate. This orientation is from here onwards referred to as 'OR I'. The other orientation, 'OR II', is present as small islands surrounded by the large OR I grain. As seen in Fig. 4b), the out-of-plane direction in the entire film is (0002). To establish the complete orientation relationship of both grains, the direction of each of the grains that is parallel to [100] of the substrate is obtained from the EBSD data shown in Fig. 4c). Using this we can determine the following orientation relationship:

OR I: $(0002)_{Ti} \parallel (001)_{SrTiO_3}$, $[5\bar{7}20]_{Ti} \parallel [100]_{SrTiO_3}$

OR II: $(0002)_{Ti} \parallel (001)_{SrTiO_3}$, $[5\bar{4}\bar{1}0]_{Ti} \parallel [100]_{SrTiO_3}$

The unique grain map shown in Fig. 4d) also confirms the presence of only two orientations. The novelty of the pulsed magnetron sputtered films is that they are not only bicrystalline, but the majority of the grains are columnar leading to a strongly textured film microstructure. We examined a cross-section TEM lamella to observe the microstructure of the film in the growth direction. As shown in Fig. 5, BF/DF TEM imaging was used to further investigate the evolution of the grain structure in growth direction. From the BF TEM image shown in Fig. 5a) it becomes apparent that nanoscale columnar grains are present near the film-substrate interface, which then transition into large near micron-sized grains at a distance of ~300 nm from the substrate. We acquired SADPs from two columnar grains with schematic locations of the apertures as indicated by green and blue circle in Fig. 5a). The SADP in Fig. 5e) is in [10$\bar{1}$0] zone axis and the SADP in Fig. 5f) is in [11$\bar{2}$0] zone axis. Both of these SADPs were acquired without stage tilt between them and the two zone axes are 30° apart which is in agreement with the orientation relationship observed using EBSD. Subsequently, dark field images shown in Fig. 5b) and c) were acquired from the two OR using the highlighted diffraction spots in Fig. 5e) and f). The SADP acquired from the columnar nanograins (d* in Fig. 5a)) shows that it is mostly a sum of the diffraction pat-

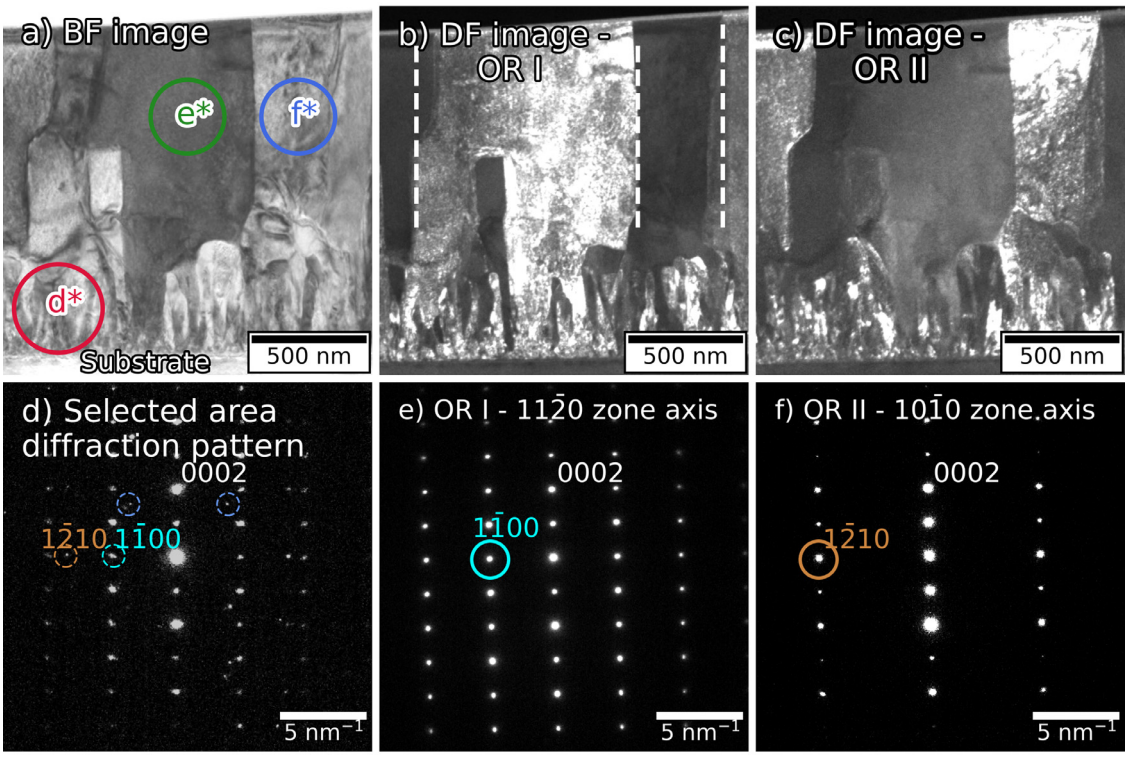


**Fig. 5.** Ti thin film deposited on $SrTiO_3$ at 600 °C and annealed at 600 °C for 8 h. a) Bright field (BF) TEM micrograph of the cross-section showing columnar grains and vertical GBs. The red, green and blue coloured circles schematically indicate the aperture locations used to acquire the selected area diffraction patterns (SADPs) seen in d), e) and f), respectively. b) Dark field (DF) TEM micrograph acquired using the 1$\bar{1}$00 reflection in e). c) Dark field TEM micrographs acquired using the 1$\bar{2}$10 reflection in f). d) SADP acquired from the smaller columnar grains next to the film-substrate interface in the film. The blue dotted circles highlight the additional reflections seen only in the interface region. e), f) SADPs acquired from the two grains corresponding to OR I and OR II, respectively. The cyan and brown circle represent the diffraction spots used to acquire the dark field micrographs. (For interpretation of the references to color in this figure legend, the reader is referred to the web version of this article.)

terns shown in Fig. 5b) and c). This indicates that most of the small columnar grains also adopt either OR I or OR II orientation. The additional reflections marked in blue in Fig. 5d) are stemming from a few in-plane rotated grains which exist only close to the film-substrate interface. To the best of our knowledge, this is the first report of a bicrystalline Ti thin film which is particularly interesting due to the challenges involved in producing a bulk Ti bicrystal.

### 3.2. Grain size and grain growth measurement

A larger in-plane grain size is seen for the films deposited by pulsed magnetron sputtering compared to the film deposited using dcMS. However, due to the maze-like microstructure of the pulsed magnetron sputtered films, the grain size distribution data has to be generated separately for OR I and OR II grains. The OR I grain is essentially one large continuous grain extending over the entire substrate, therefore, the line interception method (in the TSL OIM software) was used to measure the average width of the grain. In this method, several horizontal lines were drawn across the EBSD scan area to measure the mean intercept length (width) of the OR I grain. For the OR II grains, the equivalent circle diameter was calculated using the grain area.

The increase in width of the OR I grain as a function of annealing duration is given in Table 1. The width remains almost the same within the error limit between the 2 h and 4 h annealed films, however, it largely increases for the 8 h annealed film. Similarly, a decrease in the grain size of OR II from 2 h to 8 h is observed, due to the shrinkage of the island grains. A net increase in the grain size as a function of annealing duration can be noted by measuring the length of GB for a given area of the film. As seen in Table 1, for an area of 25 µm × 20 µm, the length of Σ13 GB reduces from 1.38 mm to 895 µm to 525 µm for 2 h, 4 h and 8 h film, respectively. It is generally considered that grain growth in thin films is arrested when the grain size is about one to two times the film thickness [49]. The driving force for grains to grow 2-dimensionally is much smaller than 3-dimensional growth. As seen from the EBSD results in Fig. 4, the GBs are meandering through the film, resulting in a low mean radius of curvature. This exerts a capillary force on the GBs to straighten them which promotes their migration towards their centre of curvature. This causes both grain growth and shrinkage in different sections of the grain. Similar phenomena have been observed in bicrystalline Au films [50].

Additionally, using the TSL-OIM software, a partition of OR I and OR II orientation is created from the acquired EBSD data for all three films deposited using pulsed magnetron sputtering. The OR II oriented grains are highlighted in blue in Fig. 6a), b) and c) for 2 h, 4 h and 8 h of annealing, respectively. As a function of annealing time, the OR I orientation grows at the expense of OR II orientation resulting in an increase in the single crystallinity percentage, as shown in Fig. 6d).

### 3.3. Grain boundary faceting

The Σ13 GBs in Figs. 3b) and 4 c) are observed to be continuously curved and to form a mazed bicrystalline microstructure. Such GB curvature is often accommodated by faceting if the inclinational dependence of the grain boundary energies is anisotropic [11,30]. Upon investigation at a higher magnification, the GBs are observed to be faceted, as seen in Fig. 7a). The plane normal of each facet plane is 30° apart from each other. A fast Fourier trans-

**Table 1**
Deposition conditions, OR I/ OR II grain size and Σ13 GB length of the pulsed magnetron sputtered films.

| Annealing temperature & time | OR I grain (intercept length-μm) | OR II grain (diameter-μm) | GB length |
|---|---|---|---|
| 600 °C & 2 h | 0.68 ± 0.55 | 5.10 ± 2.74 | 1.38 mm |
| 600 °C & 4 h | 0.60 ± 0.68 | 1.96 ± 1.18 | 895 μm |
| 600 °C & 8 h | 2.81 ± 2.53 | 1.75 ± 0.84 | 525 μm |

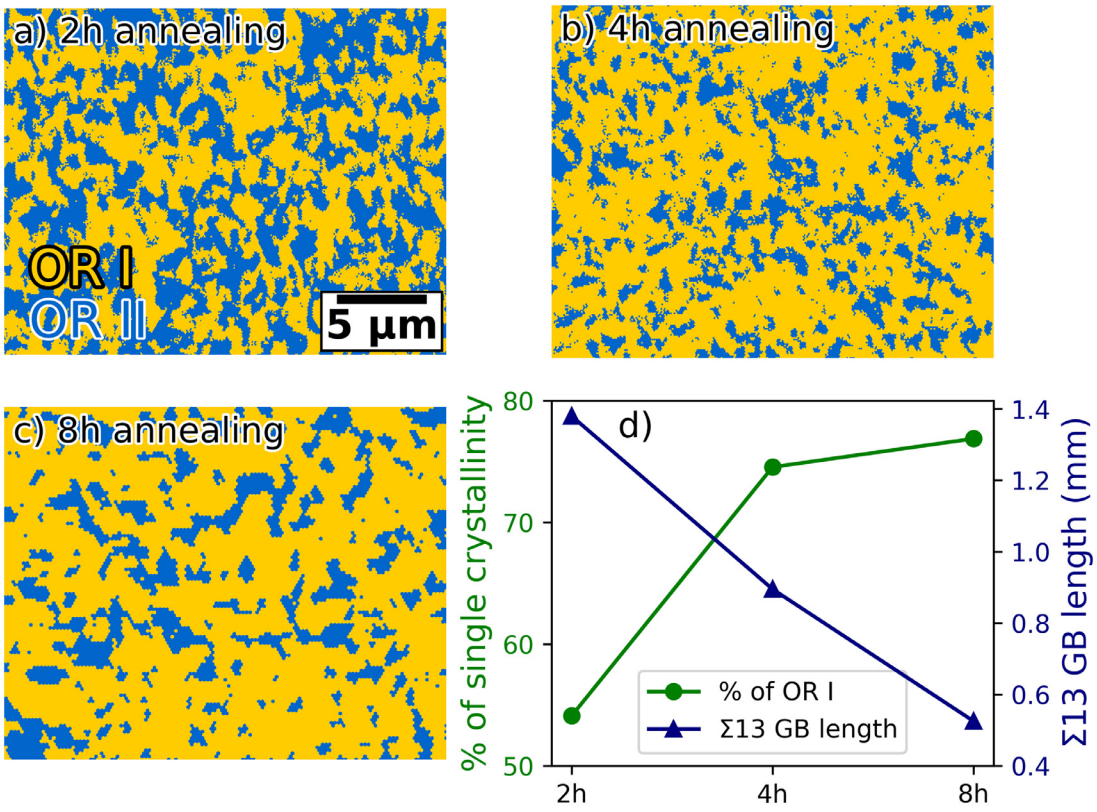


**Fig. 6.** a), b) and c) show EBSD images of pulse magnetron sputtered films deposited at 600 °C and annealed at 600 °C for 2 h, 4 h and 8 h, respectively, partitioned into OR I (yellow) and OR II (blue) grains. d) The increasing area fraction of OR I grain and the decreasing length of GB per unit area are plotted with respect to annealing duration demonstrating grain growth and increasing % of single crystallinity. (For interpretation of the references to color in this figure legend, the reader is referred to the web version of this article.)

form (FFT) of the HAADF-STEM image in Fig. 7a) can be used to index the GB planes. Because the GBs are all edge-on, as previously demonstrated in Fig. 4b), the GB planes can be indexed by simply locating the intersection of the GB plane normals to the great-circle in the (0001) stereographic projection of Ti. However, a more precise method of GB plane indexing is demonstrated in detail in the supplementary information (Fig S5). Using this method, the GB facets are indexed to be $\{\bar{7}520\}$ and $\{\bar{4}310\}$ symmetric planes. From the FFT it is also apparent that $\{\bar{7}520\}$ and $\{\bar{4}310\}$ are the only conceivable symmetric GB plane families in Σ13 [0001] hcp GBs. GB planes with any other Miller indices would be asymmetric. A preference for the symmetric GB planes is readily apparent.

In another instance, as seen in Fig. 7c), although the GB facet normals are still 30° apart, the planes were indexed to be low-index asymmetric $\{10\bar{1}0\}$ // $\{2\bar{1}\bar{1}0\}$ planes. The FFT shown in Fig. 7d) confirms the asymmetricity of the facets. According to the authors' observations, out of over ~200 μm of GB less than ~30 μm of the GB is asymmetric, which corresponds to less than ~15% of the GB being asymmetric.

### 3.4. Anisotropic Fe segregation in symmetric GB facets

Fe was present as an impurity in the sputtering target therefore it is of interest to examine where it is present in the deposited films. In the film deposited using pulse magnetron sputtering and post-annealing for 8 h at 600°, the Σ13 [0001] Ti GB is seen to be composed of $\{\bar{7}520\}$ symmetric GB facets, as shown in Fig. 8a). The facets are similar to the GB faceting discussed in Fig. 7. The elemental distribution map of Fe, acquired using STEM-EDS at 300 kV, reveals a preferential segregation of Fe to every alternate symmetric facet. However, we do not see a change in the contrast between neighbouring GB facets in the HAADF-STEM images in Fig. 7. This is because the contrast from GBs observed at lower resolution represents a superposition of various effects stemming from strain contrast due to the presence of GB defects, local sample thickness and compositional variations. The Fe present in the GB facets is not high enough to produce a clear HAADF signal under these observation conditions. For completeness, the change in GB contrast with decreasing collection angles of the annular STEM detectors is shown in Fig S3. In Fig. 8, Fe segregation is observed at $(\bar{5}7\bar{2}0)$, $(\bar{7}250)$, and $(\bar{2}\bar{5}70)$ facets, but Fe is not detected at $(\bar{4}310)$ and $(\bar{3}\bar{1}40)$ facets. The counts of the Fe signal in the EDS spectrum are integrated along the highlighted arrow over the marked region as seen in Fig. 8b). Fig. 8d) and e) show line profiles across the corresponding facets to clearly illustrate the segregation of Fe at the $(\bar{2}570)$ GB plane and the absence of Fe-segregation in the $(\bar{3}\bar{1}40)$ facet. The FWHM of the spacial distribution of Fe in Fig. 8e) is ~0.15 nm confirming the segregation of Fe is limited to the GB.

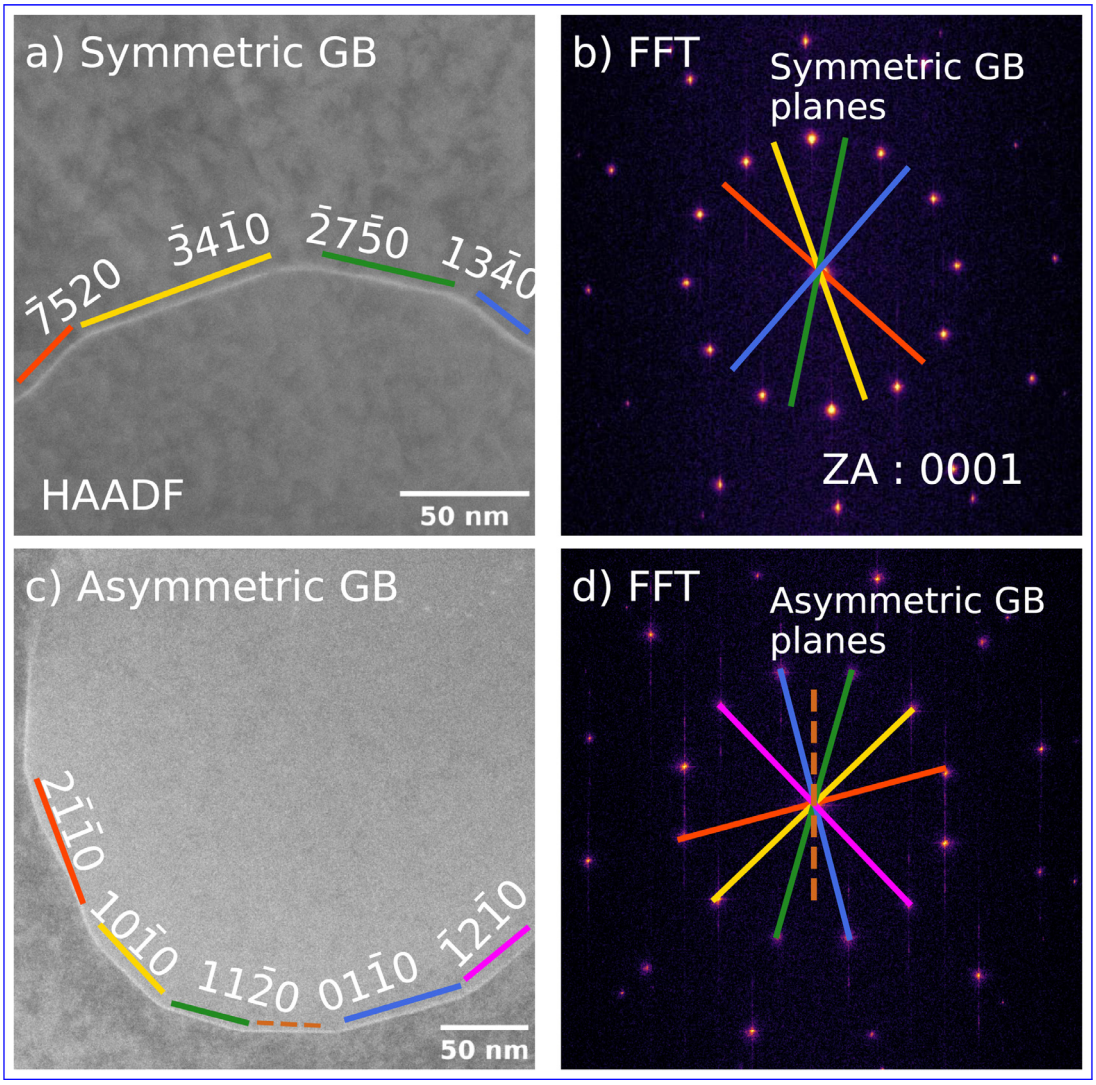


**Fig. 7.** a) HAADF-STEM image of Σ13 [0001] Ti GB in the pulsed magnetron sputtered film deposited at 600 °C and post-annealed at 600 °C for 8 h showing a faceted GB with symmetric GB facets. Each GB plane is represented by a different colour. b) Fast Fourier transform (FFT) of the HAADF-STEM image in a). c) HAADF-STEM image of from a different region showing asymmetric GB facets. d) FFT from the HAADF-STEM image shown in c). The dashed brown line is a symmetric facet present between the two asymmetric facets. (For interpretation of the references to color in this figure legend, the reader is referred to the web version of this article.)

To quantify the amount of segregation APT was used. Firstly, the GB facet containing Fe was targeted to be lifted-out using the conventional FIB sample preparation technique and field evaporated in laser-mode. After the reconstruction of data using AP Suite, the atom distribution maps of Ti and O are obtained, as shown in Fig. 9a). Both of them are seen to be distributed uniformly in both the grains and the GB region. Fe is seen in Fig. 9b), c) and d) to distinctly segregate to the GB. To delineate the Fe GB segregation, a 0.5 at.% Fe isoconcentration surface is plotted in Fig. 9b) and as seen in Fig. 9d), the GB is edge-on. A cylinder of 30 nm diameter and 50 nm length is highlighted as the selected region of interest (ROI). Although the GB extends over the entire cross-section of the APT tip, Fe is seen enriched at only a fraction of the GB area. The composition along the ROI in both Fig. 9b) and c) are plotted in Fig. 9e) and f), respectively. Negligible Fe segregation is observed in Fig. 9e) whereas significant Fe segregation of up to ∼0.5 at.% is observed in Fig. 9f). The Fe segregation is distributed to a width of ∼8 nm (FWHM <4 nm). The segregation width is significantly larger than the expected GB width due to the artefacts from field evaporation and aberrations in the trajectory of ions [51]. Nevertheless, this apparent increase of GB width is inconsequential for a homo-phase boundary as the concentration on both sides of the Gibbsian dividing surface can be considered to be identical. Although not highlighted in Fig. 9b), c) and d) for clarity, three ROIs of the same dimensions were taken for better statistics. As seen in Fig. 9g), plotting the number of Fe atoms against the total number of atoms of all elements in the region of interest allows us to measure the number of GB excess Fe atoms per unit area of the interface, $N_{Fe}$. Using the equation Eq. (1), $\Gamma_{Fe}$ is found to be 1.25 ± 0.1 atoms/nm$^2$. Since the {$\bar{7}$250} GB has ∼8–10 at/nm$^2$ (ambiguity arises because of the dependence of planar-atomic-density on the width of a high-index GB plane), the amount of segregation can also be described as ∼0.2 monolayers, assuming that the Fe segregation is limited to the GB plane. The relationship between misorientation and GB excess property measured using APT has been discussed in cubic metals [28,52], however no report for hcp metals was found in the literature. To emphasize that the segregation of Fe is limited to the GB plane, and to show its distribution, an areal density plot of Fe in the GB plane is shown in Fig. 9h).

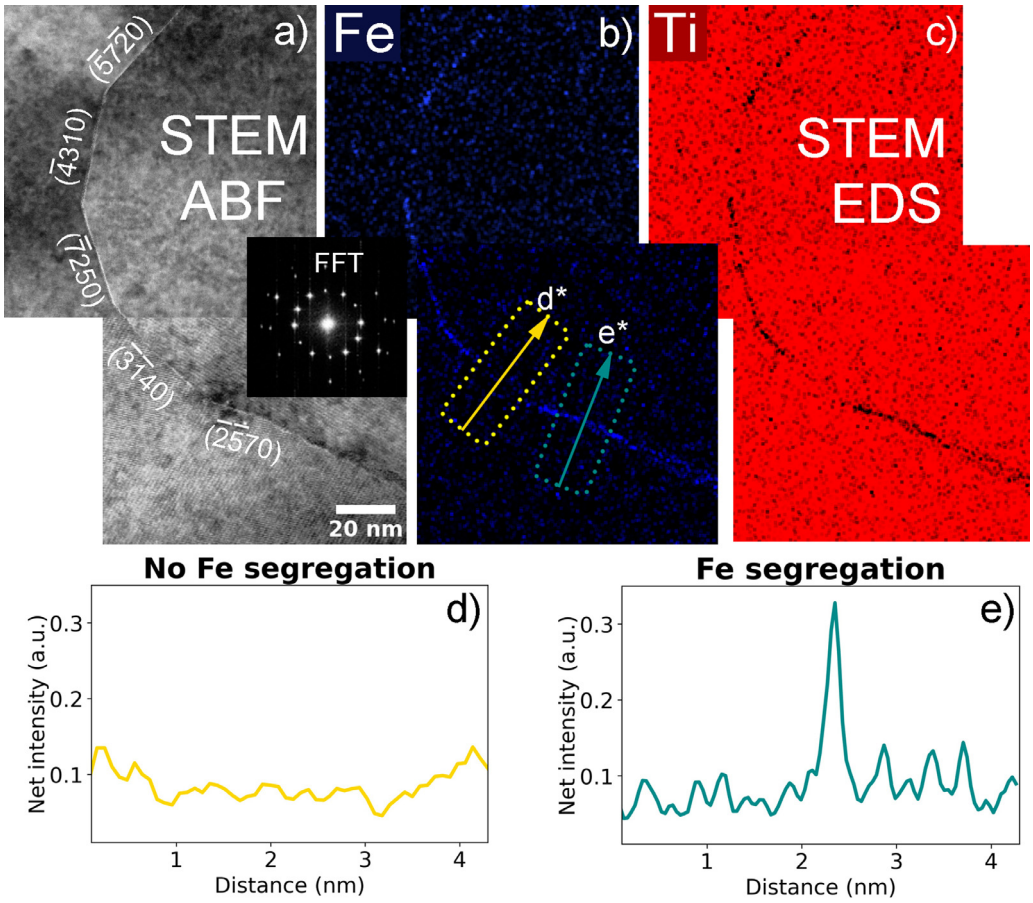


**Fig. 8.** a) STEM annular-BF image showing GB facets with symmetric {$\bar{7}520$} and {$\bar{4}310$} GB planes. EDS reveals segregation of b) Fe in alternate GB facet, c) depletion of Ti in the Fe rich region. d), e) Net-intensity line profile across the two symmetric facets revealing a strong segregation of Fe in only the {$\bar{2}\bar{5}70$} facets.

## 4. Discussion

### 4.1. Thin film deposition and texture evolution

In a plasma with a large degree of ionization, the ion flux to the substrate is larger than for discharges with a low degree of ionization [42]. The magnitude of ion current affects the morphology evolution which is evident when comparing the SE image of the film deposited by dcMS in Fig. 2a) and the SE image of the film deposited by pulsed magnetron sputtering in Fig. 3a). The incoming sputtered atoms from the target when adsorbed on the substrate surface are called adatoms. Due to the dense plasma in pulsed magnetron sputtering, adatom mobility to low surface energy sites with high coordination is promoted. Enhanced surface diffusion eliminates the voids and surface mounds and consequently reduces the surface roughness of the grown films. It also leads to a smoother surface finish [53]. Increase in surface smoothness and density of films on using higher duty cycles have been reported earlier in $TiO_x$ [38].

Additionally, the lowest surface energy plane, (0002), dominated over the lowest strain energy plane, {$10\bar{1}1$}. The high flux of ions due to pulsing leads to the increased momentum transfer between the plasma and the condensed metal atoms. Such a high flux increases the mobility of surface adatoms and accommodates them on planes of the lowest surface energy. This determined the out-of-plane surface orientation. A similar change in texture evolution in changing the deposition method from dcMS to pulsed magnetron sputtering favouring the high atomic density surface planes has also been reported in other materials [54–56].

The two in-plane orientation relationships were found using the EBSD data in Fig. 4. As seen in Fig. 5, the majority of nanocrystalline grains seems to follow an OR and hence the consideration of misfit strain becomes important. The misfit ($\delta$) can be calculated using $\delta = (1 - \frac{d_f}{d_s})$, where $d_f$ and $d_s$ are the film and substrate lattice spacing. The lattice parameter for cubic $SrTiO_3$ is a=3.9 Å. $d_{5\bar{7}20}$ and $d_{\bar{5}410}$ are 0.409 Å and 0.577 Å, respectively. Using the domain matching epitaxy (DME) paradigm [57,58], we can calculate the misfit strain for OR I in the two in-plane directions to be 4.8% and 3.5%. Because the film has hexagonal symmetry and the substrate cubic, there are two misfit values. The misfit strain for OR II is swapped with 3.5% and 4.8%, respectively, due to the 30° in-plane rotation between the two orientations. Besides lattice misfit, the residual stresses, the distribution of misfit dislocations in the interface, the surface plane termination of $SrTiO_3$ and surface irregularities are possible other factors that can influence the evolving OR. Fig. S6 shows STEM-EDS measurements performed at the film-substrate interface. Since there are no other elements detected within the substrate-film interface within the detection limit of STEM-EDS, it is concluded that the contrast modulations in Fig. 3 d) stem mainly from diffraction contrast of the nanocrystalline layer.

All pulsed magnetron sputtered films were observed to have columnar grains. This can be explained using the structure zone model (SZM). The SZM is commonly used to determine the dependence of film microstructure on the discharge pressure and the homologous temperature [59]. The film microstructure according to this model is categorized into four zones, namely Zone 1, Zone T, Zone 2, and Zone 3 based on the substrate temperature during de-

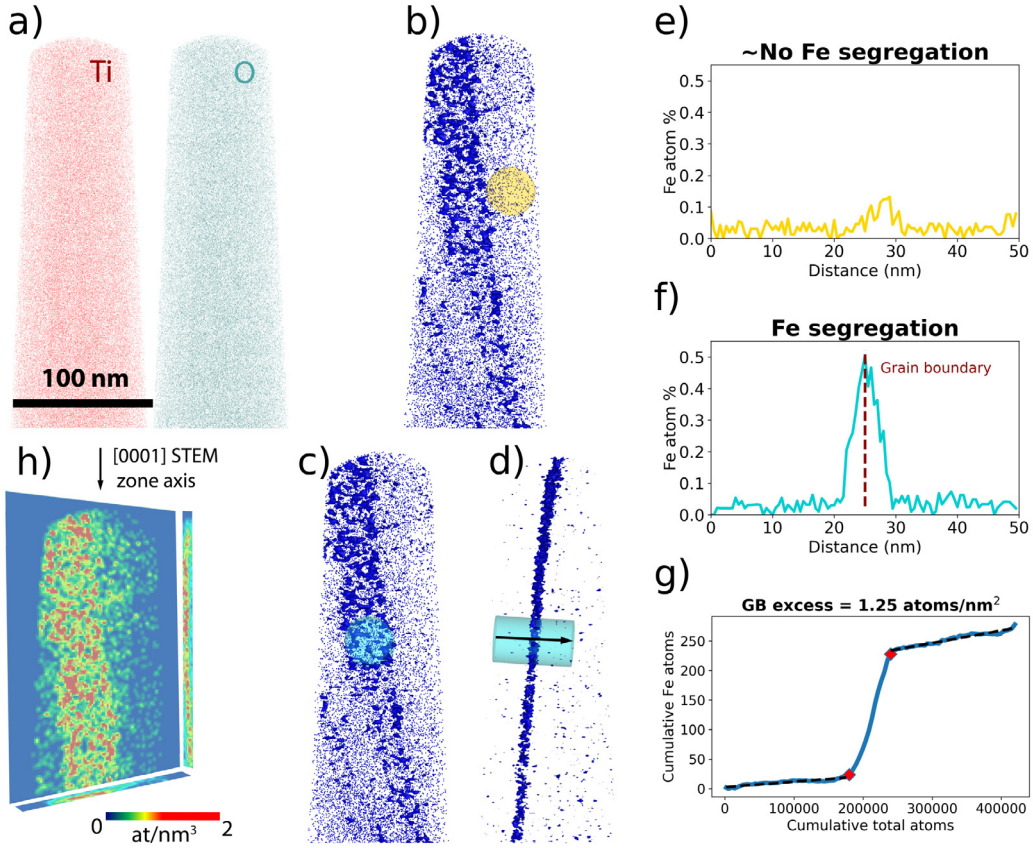


**Fig. 9.** a) Reconstruction point cloud from APT showing Ti and O atoms marked in red and green, respectively. b) Isoconcentration surface of 0.5 at.% Fe delineates the GB and demonstrates the segregation limited to a fraction of the GB area present in the tip. The region of interest (ROI) used for composition analysis through the GB segment having no Fe segregation is highlighted (in yellow). c), d) ROI passing through the Fe-enriched GB region is depicted in both front and side view, respectively (in teal). e), f) show composition profiles from ROI exhibiting ~no Fe segregation (b) and Fe-segregation (c), respectively. g) Ladder diagram of Fe and obtained Gibbsian GB excess following [44]. h) The in-plane atomic density distribution of Fe in the GB plane. (For interpretation of the references to color in this figure legend, the reader is referred to the web version of this article.)

position. Zone T has limited surface diffusion and grain boundary mobility. This leads to 'V' shaped columnar grains where the grains with lower surface energy compete with other orientations during grain growth. In the Zone II, due to increased surface diffusion, the preferred orientations nucleate at the substrate surface and grow as columnar grains. This leads to near vertical GBs [60]. A detailed discussion on the model can be found in [60,61]. In the present film, the deposition temperature of 600 °C lies in the early Zone II ($T_s$ / $T_m$ ~ 0.45; $T_s$: deposition T, $T_m$: melting point of target). As expected from the SZM, the cross-section observations of the films indicate that the films belong to Zone II and Zone T in Fig. 5. The BF/DF micrographs reveal that most of the GBs are vertical. In columnar grain growth the favourably oriented grains quickly eliminate the less favourably oriented grains [62]. Therefore, only OR I and OR II grains remain at ~300 nm above the film-substrate interface. The most important consequence of this is that almost all the GBs can be identified as Σ13.

Due to the mazed bicrystalline microstructure, the GB plane changes continuously but the GB is characterized by the same disorientation. High-resolution STEM imaging was used to identify the GB planes because even a detailed EBSD scan with a step size of <10 nm is not sufficient to index such finely faceted/rounded GBs.

### 4.2. Grain boundary faceting

Faceting is the dissociation of a GB into segments with different GB plane inclination but the same overall misorientation. It principally occurs to reduce the overall GB energy. The total energy of a faceted GB is the sum of the energy of individual GB segments and their interaction energy at the facet junctions. As faceting leads to an increase in GB plane area, the facets must have lower energy than the parent GB for faceting to occur. Although GB faceting has been widely reported in many cubic metals [63–65], to the best of the authors' knowledge, no experimental evidence of GB faceting has been reported for Ti. Here, we show that the GB plane which would otherwise be asymmetric due to its continuous curvature, dissociates into distinct facets.

Since all grains are columnar, it is evident that all the GBs in a basal-plane textured film are prismatic in nature. Moreover, there is a competition between the low index asymmetric prismatic $\{10\bar{1}0\}$ // $\{2\bar{1}\bar{1}0\}$ GB planes and the symmetric prismatic $\{\bar{7}520\}$ and $\{\bar{4}310\}$ GB planes. The prismatic planes have been shown to be the preferred GB facet plane in other hcp materials [66,67]. A 3D-EBSD study on bulk-Ti reported a large fraction of grains with misorientation $\leq 30^\circ$ having prismatic GB planes with a preference for $\{\bar{7}520\}$ [67]. Therefore, not only are the $\{\bar{7}520\}$ GBs preponderant in thin films, but they are also frequently observed in the bulk commercially pure Ti. Also, prismatic planes are preferred in the $\beta \rightarrow \alpha$ martensitic phase transformation in Ti [68]. The $\{\bar{7}520\}$ prismatic planes are also predominant in Σ13 [0001] GBs in Mg [69]. Using atomistic calculations, Ostapovets et al. were able to show that the minima of [0001] tilt GB energy corresponds to $\{\bar{7}520\}$ [69]. Although, similar GB energy calculations via MD simulation for Ti [0001] tilt-GBs are missing, it is expected that Ti could follow a similar trend as in Mg. Therefore, the observed GB faceting in Figs. 7a) and 8 into $\{\bar{7}520\}$ and $\{\bar{4}310\}$ symmetric segments can

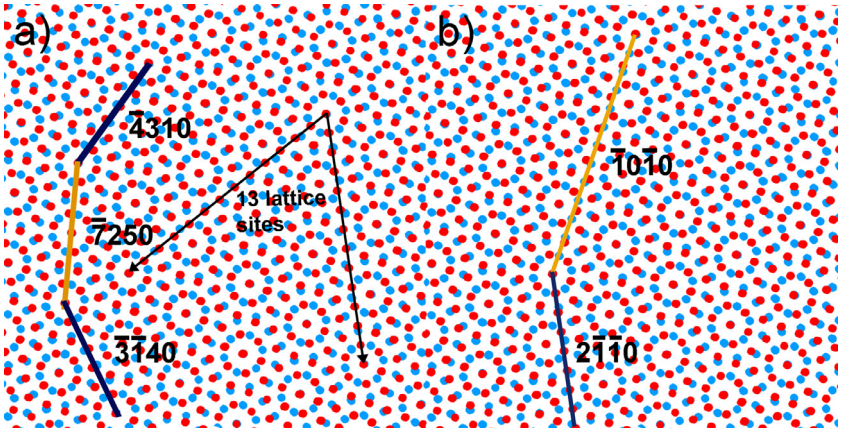


**Fig. 10.** Schematic dichromatic pattern of the Σ13 GB with a) {$\bar{7}$520} and {$\bar{4}$310} planes consisting of the highest and the second highest planar coincident site density (PCSD), respectively, and b) {$2\bar{1}\bar{1}0$} and {$10\bar{1}0$} planes with lower PCSD but higher effective d-spacing ($d_{eff}$). The arrows point that any coincident site is 13 lattice sites away from another coincident site along the [$10\bar{1}0$] direction.

be considered to be a result of the GB energy-minimization in hcp materials.

To develop a thermodynamic understanding of the GB plane selection during faceting and anisotropic segregation of Fe observed in Fig. 8, it is necessary to reveal the atomic structure and the local energetics of the particular GB. The atomic structure investigation is beyond the scope of the present study but a simple approach to rationalize the observations can be used. The CSL model is the most widely applied tool for classifying GBs. It distinguishes grain misorientations that place a large fraction of the lattice sites of the two grains in coincidence from the remaining 'general' misorientations. The sigma value represents the inverse of the number of the coinciding sites. If the GB plane passes through the coinciding points, then such a GB plane can have low energy. The term, 'planar coincident site density' (PCSD) is used to quantify the density of CSL sites on the GB plane. In a $SrTiO_3$ Σ3 (111) twist boundary, the high PCSD was held responsible for the observed GB plane [70]. To illustrate the role of PCSD in GB plane selection, a dichromatic pattern of hcp (0001) is drawn in Fig. 10. The ($\bar{7}$520) symmetric plane that is highlighted in 'gold' has the highest PCSD, $\Gamma = 0.42$, in Σ13 [0001] hcp GBs. This is followed by the ($\bar{3}4\bar{1}0$) plane highlighted in 'dark-blue' which has a $\Gamma = 0.32$.

Additionally, when considering the prismatic plane with the smallest Miller indices, {$2\bar{1}\bar{1}0$} and {$10\bar{1}0$} can be seen to have a much lower PCSD in Fig. 10b). However, the selection of GB planes cannot be entirely described by PCSD. In several cubic materials, no dependence of GB plane selection on PCSD is seen [70]. In brass and nickel, a systematic GB plane analysis demonstrated that the dependence of interplanar spacing of the GB planes, $d_{eff}$, is the more critical criterion than PCSD in the selection of the GB planes [71]. For a symmetric GB, the $d_{eff}$ is same as the d-spacing of the GB plane, while for an asymmetric GB, the $d_{eff}$ is given by:

$$d_{eff} = \frac{(d_1 + d_2)}{2} \tag{2}$$

where $d_1$ and $d_2$ are the d-spacing of the GB planes for each grain. The $d_{eff}$ is a means to generalize the d-spacing criterion for the asymmetric boundaries [72]. The energy of an unrelaxed boundary increases as the d-spacing decreases, because the atoms with the shortest d-spacing contribute the most to the boundary energy. Consequently, low-index GB planes due to their larger d-spacing are preferred [73]. In terms of probability, there are many possible asymmetric GBs and limited symmetric GBs. However, once the low-index plane for one grain is fixed, the index of the other plane is constrained by the misorientation. As a result, most asymmetric GBs have a low $d_{eff}$ and are hence unfavorable. This is why symmetric GB planes appear more frequently than random distribution.

For the Σ13 GB, the two symmetric GB planes {$\bar{4}$310} and {$\bar{7}$520} have a d-spacing of 0.709 Åand 0.409 Å, respectively. The d-spacing of GBs with {$10\bar{1}0$} and {$2\bar{1}\bar{1}0$} habit planes is larger with 2.55 Å and 1.475 Å, respectively. However, they typically form asymmetric GB variants with {$10\bar{1}0$} // {$15\bar{7}80$} habit planes leading to a smaller $d_{eff}$ of 1.421 Å. Despite the fact that the asymmetric GBs exhibit a larger $d_{eff}$ than the symmetric GBs, GBs with {$\bar{7}$520} and {$\bar{4}$310} habit planes are observed more frequently in the present study, but also in Mg and Ti-64 alloys [67,69]. This confirms that other than the PCSD and d-spacing, the atomic structure of the GBs and their related excess thermodynamic properties influence the GB plane selection. It is well established that GBs act as a 'phase' in themselves and have an atomic structure that is distinct from the two abutting grains [74,75]. In all of existing literature that discusses the rules for selection of the GB [70,71,73], the atomic structure of GB has never been taken into consideration. However, the structure of the GB can play a major role in determining its thermodynamic properties. The structure of the GB would also determine its ability to accommodate defects, equilibrium solute segregation and their influence on the GB energy. Therefore, although a combination of PCSD and $d_{eff}$ can be used to argue the stability of certain GB planes, further investigation of the atomic structure of the {$\bar{7}$520} is needed to establish the reason for stability of the high-index symmetric GB plane over the low-index asymmetric plane, which is an ongoing work.

### 4.3. Grain boundary segregation

Solute segregation at GBs is known to largely influence the mechanical behaviour of metals either negatively, such as by embrittlement, or positively, by pinning the GBs and thus restricting grain growth, thereby strengthening it [76–78]. Solute segregation can also lead to faceting of the GB [79,80].

Grain boundary segregation in dilute binary alloys following monolayer-type segregation is typically described by the Langmuir-McLean isotherm under equilibrium conditions [81,82]. This model does not consider solute interactions, which was introduced by Fowler and Guggenheim by treating the grain boundary as a regular solution [83]. Other statistical thermodynamics based models have been proposed to calculate the enthalpy and entropy of segregation explicitly [84–86].

The segregation of Fe in Ti has been studied in random high angle GBs by Aksyonov et al. Using density functional theory (DFT)

calculations they showed that the difference between solution enthalpy for Fe to segregate in a substitutional site and an octahedral site is minimal. Fe segregation was noted to stabilize the GBs by reducing their energy by more than 200 mJ/m$^2$ [25]. Fe segregation has also been reported in commercial Ti alloys with no analysis of the influence of GB type on the segregation behaviour [26,87,88]. In the present study, Fe was observed to segregate preferentially to selected symmetric facets in Σ13 (0001) Ti GB, as seen in Fig. 8. The observed anisotropic segregation behavior of Fe is to a first approximation rationalized using the d-spacing. The GB planes ($\bar{4}$310) and ($\bar{3}\bar{1}$40) have a higher d-spacing and are seen to have lean or no segregation whereas, the GB planes ($\bar{5}7\bar{2}$0), ($\bar{7}$250), and ($\bar{2}\bar{5}$70) have a lower d-spacing and have much higher Fe segregation. Clearly, a lower d-spacing seems to favour Fe solute segregation in Ti.

Beyond characterizing the GB plane, it is of great interest to quantify the amount of segregation. Such studies began in the early 1980s using surface analysis techniques like Auger electron spectroscopy (AES) and secondary ion mass spectroscopy (SIMS) of fracture surfaces [83,89–91]. With the manifold advancement of the analytical power of STEM, EDS and electron energy loss spectroscopy (EELS) are now regularly used to quantify the lean segregation of even less than 0.01 monolayer at the GB [92,93,93,94]. More recently, state-of-the-art STEM techniques and atom probe tomography have been utilized in a correlative fashion to obtain spatial and chemical information from the same region down to almost atomic scale [28,52,95–98]. A similar approach was used here to site specifically lift-out a symmetric GB and quantify the Fe segregation as seen in Fig. 9. Although, the EDS clearly shows Fe segregation and partitioning to different GB segments, it needs however long counting times and thus may cause redistribution of Fe like seen in other metallic systems [99]. Therefore, APT is used for the quantification of solute concentration. Additionally, the distribution of concentration in the third-dimension cannot be obtained in the STEM-EDS. It also helps to find any additional scarce impurity present in the material. From the atom distribution in Fig. 9, a uniform distribution of Ti and O is confirmed. Although the concentration of O is high, ∼28 at.%, it is measured to be uniformly distributed over the entire tip volume. The high O content in the film is due to the high solubility limit (32 at.%) of O in Ti [100,101]. Because the deposition chamber had a vacuum of only $2.2 \times 10^{-6}$ mbar, and Ti is widely used as a getter for O, the film is expected to have a high dissolved O content. However, no oxides or other secondary phases are detected. Most importantly, the distribution of O is not altered at the GB and can therefore be assumed to not have an influence on the Fe segregation. Although the GB plane cannot be found from the APT data, we know that the film has mostly Σ13 GBs, with only two possible GB planes. As discussed earlier, the symmetric {$\bar{7}$250} and {$\bar{4}$310} GBs are present ∼20 times more often than the (10$\bar{1}$0) / (11$\bar{2}$0) asymmetric variant, therefore we assume the captured GB to be a symmetric GB. Furthermore, the Fe distribution is restricted to ∼40–50 nm, which is about the same as the length of symmetric facet. Combining the results of STEM and APT, it is likely that two of the symmetric GB facets, for example {$\bar{2}\bar{5}$70} and {$\bar{3}\bar{1}$40}, were captured within our atom probe tip. While the former has a rich and uniform Fe distribution, the latter is lean in Fe. The area density distribution map in Fig. 9h) distinctly shows that Fe is uniformly distributed in an area corresponding to one GB segment. The decrease in the density of the Fe in the right part of the GB can be attributed to the commencement of the adjacent facet that is lean in Fe. A striking similarity suggesting that Fe-segregation is restricted to symmetric GB segments can be seen in both Fig. 8d), e) and 9 e), f).

The subsequent measurement of interfacial excess using a 'ladder diagram' gave a $\Gamma_{Fe}$ of 1.25 at/nm$^2$ or 0.2 monolayer. The $GB_{excess}$ measurement has been used as a method to scrutinize phase formation in the GBs [102]. 0.2 monolayer corresponds to one in every five atoms at the GB plane being Fe. With the spatial resolution of APT, there is no way to ascertain if the present observation is GB segregation (either by strain or chemically induced by bonding/charge transfer) or a GB phase transformation. Based on the local arrangement and bonding of Fe, its influence on the material properties could largely vary. This necessitates the requirement of additional experiments using STEM to discern the atomic structure of the GB with and without Fe, which is an ongoing work.

## 5. Conclusion

Following the deposition of bicrystalline Ti thin films, the faceting and Fe-segregation in Σ13 [0001] GBs of Ti thin films are explored here for the first time. Following are the important findings from this work:

1. A novel template based thin film deposition pathway for obtaining columnar grains containing tilt GBs of Ti is established using pulsed magnetron sputtering on $SrTiO_3$ (001) substrates at 600°C followed by post-annealing at the same temperature for 2 h, 4 h and 8 h.
2. The ion current density during magnetron sputtering is seen to modify the texture from a mixture of (10$\bar{1}$1) and (0002) to only (0002).
3. EBSD and TEM analysis reveals a bicrystalline film with continuously curved GBs having a very high fraction of Σ13 [0001] CSL GBs. Such a textured film with well defined CSL GBs is demonstrated for the first time.
4. Two orientation relationships (ORs) are identified, where OR I is one continuous grain spread over the entire substrate. The OR II grains are distributed across the film and are observed to shrink upon annealing of the films. The two ORs are given as:
   OR I: $(0002)_{Ti} \parallel (001)_{SrTiO_3}$, $[5\bar{7}20]_{Ti} \parallel [100]_{SrTiO_3}$
   OR II: $(0002)_{Ti} \parallel (001)_{SrTiO_3}$, $[5\bar{4}\bar{1}0]_{Ti} \parallel [100]_{SrTiO_3}$
5. (S)TEM imaging revealed GBs faceted frequently into symmetric {$\bar{7}$520} and {$\bar{4}$310}, and sporadically asymmetric {10$\bar{1}$0} // {2$\bar{1}\bar{1}$0} facets. The selection of GB planes during faceting is considered to be a combination of high planar coincidence site density and high effective interplanar spacing ($d_{eff}$).
6. EDS analysis reveals a distinct preferential Fe segregation in every {$\bar{7}$520} GB facet while every {$\bar{4}$310} GB remains Fe-lean. A similar behavior was verified by atom probe tomography and the Fe solute excess at the Fe-rich facets was determined to be 1.25 at/nm$^2$.

## Declaration of Competing Interest

The authors declare that they have no known competing financial interests or personal relationships that could have appeared to influence the work reported in this paper.

## Acknowledgement

VD and CHL acknowledge the funding from KSB Stifftung. GD acknowledges funding from the European Research Council (Grant no. 787446-GB-CORRELATE). The authors would like to thank Dr. Baptiste Gault for his assistance with the APT experiments.

## Supplementary material

Supplementary material associated with this article can be found, in the online version, at doi:10.1016/j.actamat.2022.118180.

## References


[1] R.R. Boyer, An overview on the use of titanium in the aerospace industry, Mater. Sci. Eng. A 213 (1) (1996) 103–114, doi:10.1016/0921-5093(96)10233-1.

[2] D. Banerjee, J.C. Williams, Perspectives on titanium science and technology, Acta Mater. 61 (3) (2013) 844–879, doi:10.1016/j.actamat.2012.10.043.

[3] M. Peters, J. Hemptenmacher, J. Kumpfert, C. Leyens, Structure and Properties of Titanium and Titanium Alloys, John Wiley 'I&' Sons, Ltd, 2003, pp. 1–36.

[4] S. Banerjee, P. Mukhopadhyay, Phases and Crystal Structures, in: Pergamon Materials Series, vol. 12, Pergamon, 2007, pp. 1–86.

[5] D. Pan, B. Liu, R. Xu, J. Qiu, C. Liu, Predicting workability of a low-cost powder metallurgical Ti-5Al-2Fe-3Mo alloy using constitutive modeling and processing map, Materials 14 (4) (2021), doi:10.3390/ma14040836.

[6] Y. Peng, Q. Zhu, T. Luo, J. Cao, Enhancement of the tensile strength by introducing alloy element Fe for Ti based alloy, Solid State Commun. 318 (2020) 113982, doi:10.1016/j.ssc.2020.113982.

[7] E. Reverte, S.A. Tsipas, E. Gordo, Oxidation and corrosion behavior of new low-cost Ti-7Fe-3Al and Ti-7Fe-5Cr alloys from titanium hydride powders, Metals 10 (2) (2020), doi:10.3390/met10020254.

[8] A. Devaraj, V.V. Joshi, A. Srivastava, S. Manandhar, V. Moxson, V.A. Duz, C. Lavender, A low-cost hierarchical nanostructured beta-titanium alloy with high strength, Nat. Commun. 7 (2016) 1–8, doi:10.1038/ncomms11176.

[9] A. Bläsius, U. Gonser, Precision phase analysis, Le J. Phys. Colloques 37 (C6) (1976) C6–397, doi:10.1051/jphyscol:1976677.

[10] I. Levi, D. Shechtman, The microstructure of rapidly solidified Ti-Fe melt-spun ribbons, Metall. Trans. A 20 (12) (1989) 2841–2845, doi:10.1007/BF02670176.

[11] B.B. Straumal, A.R. Kilmametov, Y. Ivanisenko, A.S. Gornakova, A.A. Mazilkin, M.J. Kriegel, O.B. Fabrichnaya, B. Baretzky, H. Hahn, Phase transformations in Ti-Fe alloys induced by high-pressure torsion, Adv. Eng. Mater. 17 (12) (2015) 1835–1841, doi:10.1002/adem.201500143.

[12] B.B. Straumal, A.R. Kilmametov, Y. Ivanisenko, A.A. Mazilkin, R.Z. Valiev, N.S. Afonikova, A.S. Gornakova, H. Hahn, Diffusive and displacive phase transitions in Ti-Fe and Ti-Co alloys under high pressure torsion, J. AlloysCompd. 735 (2018) 2281–2286, doi:10.1016/j.jallcom.2017.11.317.

[13] A. Kilmametov, Y. Ivanisenko, B. Straumal, A.A. Mazilkin, A.S. Gornakova, M.J. Kriegel, O.B. Fabrichnaya, D. Rafaja, H. Hahn, Transformations of $\alpha$' martensite in Ti-Fe alloys under high pressure torsion, Scr. Mater. 136 (2017) 46–49, doi:10.1016/j.scriptamat.2017.04.010.

[14] A.R. Kilmametov, Y. Ivanisenko, A.A. Mazilkin, B.B. Straumal, A.S. Gornakova, O.B. Fabrichnaya, M.J. Kriegel, D. Rafaja, H. Hahn, The $\alpha\omega$ and $\beta\omega$ phase transformations in Ti-Fe alloys under high-pressure torsion, Acta Mater. 144 (2018) 337–351, doi:10.1016/j.actamat.2017.10.051.

[15] M.J. Kriegel, A. Kilmametov, V. Klemm, C. Schimpf, B.B. Straumal, A.S. Gornakova, Y. Ivanisenko, O. Fabrichnaya, H. Hahn, D. Rafaja, Thermal stability of athermal $\omega$-Ti(Fe) produced upon quenching of $\beta$-Ti(Fe), Adv. Eng. Mater. 21 (1) (2019) 1800158, doi:10.1002/adem.201800158.

[16] M.J. Kriegel, M. Rudolph, A. Kilmametov, B.B. Straumal, J. Ivanisenko, O. Fabrichnaya, H. Hahn, D. Rafaja, Formation and thermal stability of $\omega$-Ti(Fe) in $\alpha$-phase-based Ti(Fe) alloys, Metals 10 (3) (2020), doi:10.3390/met10030402.

[17] H. Zhao, F. De Geuser, A. Kwiatkowski da Silva, A. Szczepaniak, B. Gault, D. Ponge, D. Raabe, Segregation assisted grain boundary precipitation in a model Al-Zn-Mg-Cu alloy, Acta Mater. 156 (2018) 318–329, doi:10.1016/j.actamat.2018.07.003.

[18] A.G. Illarionov, A.S. Ushakova, F.V. Vodolazsky, ThermoCalc modelling of the effect of chemical composition on the phase transformations temperatures of Ti-0.4Al Alloy, IOP Conf. Ser. Mater. Sci.Eng. 969 (2020) 012029, doi:10.1088/1757-899x/969/1/012029.

[19] G.K. Sujan, Z. Pan, H. Li, D. Liang, N. Alam, An overview on TiFe intermetallic for solid-state hydrogen storage: microstructure, hydrogenation and fabrication processes, Crit. Rev. Solid State Mater.Sci. 45 (5) (2020) 410–427, doi:10.1080/10408436.2019.1652143.

[20] D.G. Savvakin, A. Carman, O.M. Ivasishin, M.V. Matviychuk, A.A. Gazder, E.V. Pereloma, Effect of iron content on sintering behavior of Ti-V-Fe-Al near-$\beta$ titanium alloy, Metal. Mater. Trans. A 43 (2) (2012) 716–723, doi:10.1007/s11661-011-0875-9.

[21] S. Raynova, F. Yang, L. Bolzoni, The effect of thermomechanical treatments on the properties of powder metallurgy Ti–5Fe alloy, Mater. Sci. Eng. A 801 (2021) 140389, doi:10.1016/j.msea.2020.140389.

[22] J. Matyka, F. Faudot, J. Bigot, Study of iron solubility in $\alpha$ titanium, Scr. Metall. 13 (7) (1979) 645–648, doi:10.1016/0036-9748(79)90126-1.

[23] E. Raub, C.J. Raub, E. Röschel, V.B. Compton, T.H. Geballe, B.T. Matthias, The $\alpha$-Ti-Fe solid solution and its superconducting properties, J. Less Common Metals 12 (1) (1967) 36–40, doi:10.1016/0022-5088(67)90066-5.

[24] D.A. Aksyonov, T. Hickel, J. Neugebauer, A.G. Lipnitskii, The impact of carbon and oxygen in alpha-titanium: ab initio study of solution enthalpies and grain boundary segregation, J. Phys. 28 (38) (2016) 385001.

[25] D.A. Aksyonov, A.G. Lipnitskii, Solubility and grain boundary segregation of iron in hcp titanium: a computational study, Comput. Mater. Sci. 137 (2017) 266–272, doi:10.1016/j.commatsci.2017.05.034.

[26] M.J. Bermingham, S.D. McDonald, D.H. StJohn, M.S. Dargusch, Segregation and grain refinement in cast titanium alloys, J. Mater. Res. 24 (4) (2009) 1529–1535, doi:10.1557/jmr.2009.0173.

[27] M. Simonelli, D.G. McCartney, P. Barriobero-Vila, N.T. Aboulkhair, Y.Y. Tse, A. Clare, R. Hague, The influence of iron in minimizing the microstructural anisotropy of Ti-6Al-4V produced by laser powder-bed fusion, Metal. Mater. Trans. A 51 (5) (2020) 2444–2459, doi:10.1007/s11661-020-05692-6.

[28] X. Zhou, X.-x. Yu, T. Kaub, R.L. Martens, G.B. Thompson, Grain boundary specific segregation in nanocrystalline Fe(Cr), Sci. Rep. 6 (1) (2016) 34642, doi:10.1038/srep34642.

[29] S.M. Schwarz, E.C. Houge, L.A. Giannuzzi, A.H. King, Bicrystal growth and characterization of copper twist grain boundaries, J. Cryst. Growth 222 (1) (2001) 392–398, doi:10.1016/S0022-0248(00)00918-0.

[30] U. Dahmen, K.H. Westmacott, TEM characterization of grain boundaries in mazed bicrystal films of aluminum, MRS Proc. 229 (1991) 167, doi:10.1557/PROC-229-167.

[31] K.H. Westmacott, S. Hinderberger, U. Dahmen, Physical vapour deposition growth and transmission electron microscopy characterization of epitaxial thin metal films on single-crystal Si and Ge substrates, Philos. Mag. A 81 (6) (2001) 1547–1578, doi:10.1080/01418610108214362.

[32] G. Dehm, H. Edongué, T.A. Wagner, S.H. Oh, E. Arzt, Obtaining different orientation relationships for Cu Films grown on (0001) $\alpha$-$Al_2O_3$ substrates by magnetron sputtering, Zeitschrift Fur Metallkunde 96 (2005) 249–254, doi:10.3139/146.101027.

[33] T. Radetic, C. Ophus, D.L. Olmsted, M. Asta, U. Dahmen, Mechanism and dynamics of shrinking island grains in mazed bicrystal thin films of Au, Acta Mater. 60 (20) (2012) 7051–7063, doi:10.1016/j.actamat.2012.09.012.

[34] P.M. Kluge-Weiss, C.L. Bauer, Characterization of [001] tilt boundaries in bicrystalline thin films of copper, physica status solidi (a) 58 (2) (1980) 333–341, doi:10.1002/pssa.2210580202.

[35] F. Cosandey, C.L. Bauer, Faceting of [001] grain boundaries in bicrystalline thin films of gold, Acta Metall. 28 (5) (1980) 601–605, doi:10.1016/0001-6160(80)90126-1.

[36] F. Cosandey, C.L. Bauer, 4 - characterization of grain boundaries in bicrystalline thin films, in: K.N. Tu, R. Rosenberg (Eds.), Preparation and Properties of Thin Films, Treatise on Materials Science & Technology, vol. 24, Elsevier, 1982, pp. 113–161.

[37] I. Yamada, H. Usui, S. Tanaka, U. Dahmen, K.H. Westmacott, Atomic resolution study of the structure and interface of aluminum films deposited epitaxially on silicon by ionized cluster beam method, J. Vac. Sci. Technol. A 8 (3) (1990) 1443–1446.

[38] K. Sarakinos, J. Alami, M. Wuttig, Process characteristics and film properties upon growth of $TiO_x$ films by high power pulsed magnetron sputtering, J. Phys. D 40 (7) (2007) 2108–2114, doi:10.1088/0022-3727/40/7/037.

[39] F.J. Jing, T.L. Yin, K. Yukimura, H. Sun, Y.X. Leng, N. Huang, Titanium film deposition by high-power impulse magnetron sputtering: Influence of pulse duration, Vacuum 86 (12) (2012) 2114–2119, doi:10.1016/j.vacuum.2012.06.003.

[40] D.L. Ma, Y.T. Li, Q.Y. Deng, B. Huang, Y.X. Leng, N. Huang, Tailoring the texture of titanium thin films deposited by high-power pulsed magnetron sputtering, Int. J. Mod. Phys. B 33 (01–03) (2019) 1940017, doi:10.1142/S0217979219400174.

[41] S. Konstantinidis, J.P. Dauchot, M. Ganciu, A. Ricard, M. Hecq, et al., Influence of pulse duration on the plasma characteristics in high-power pulsed magnetron discharges, J. Appl. Phys. 99 (1) (2006), doi:10.1063/1.2159555.

[42] J.M. Schneider, S. Rohde, W.D. Sproul, A. Matthews, Recent developments in plasma assisted physical vapour deposition, J. Phys. D 33 (18) (2000) R173–R186, doi:10.1088/0022-3727/33/18/201.

[43] G. Greczynski, S. Mrz, L. Hultman, J.M. Schneider, Venting temperature determines surface chemistry of magnetron sputtered TiN films, Appl. Phys. Lett. 108 (4) (2016) 041603, doi:10.1063/1.4940974.

[44] B.W. Krakauer, D.N. Seidman, Absolute atomic-scale measurements of the Gibbsian interfacial excess of solute at internal interfaces, Phys. Rev. B 48 (1993) 6724–6727, doi:10.1103/PhysRevB.48.6724.

[45] J.E. Hilliard, Estimating grain size by the intercept method, Metal Prog. 85 (5) (1964) 99–102.

[46] R. Checchetto, Titanium thin film deposition in a deuterium atmosphere, Thin Solid Films 302 (1997) 77–83, doi:10.1557/JMR.1999.0265.

[47] S. Zaefferer, Application of orientation microscopy in SEM and TEM for the study of texture formation during recrystallisation processes, in: Textures of Materials - ICOTOM 14, in: Materials Science Forum, vol. 495, Trans Tech Publications Ltd, 2005, pp. 3–12.

[48] D.G. Brandon, The structure of high-angle grain boundaries, Acta Metall. 14 (11) (1966) 1479–1484.

[49] J.E. Palmer, C.V. Thompson, H.I. Smith, Grain growth and grain size distributions in thin germanium films, J. Appl. Phys. 62 (6) (1987) 2492–2497, doi:10.1063/1.339460.

[50] T. Radetic, C. Ophus, D.L. Olmsted, M. Asta, U. Dahmen, Mechanism and dynamics of shrinking island grains in mazed bicrystal thin films of Au, Acta Mater. 60 (20) (2012) 7051–7063, doi:10.1016/j.actamat.2012.09.012.

[51] M.K. Miller, M.G. Hetherington, Local magnification effects in the atom probe, Surf. Sci. 246 (1) (1991) 442–449, doi:10.1016/0039-6028(91)90449-3.

[52] A. Stoffers, O. Cojocaru-Mirédin, W. Seifert, S. Zaefferer, S. Riepe, D. Raabe, Grain boundary segregation in multicrystalline silicon: correlative characterization by EBSD, EBIC, and atom probe tomography, Progress Photovolt. 23 (12) (2015) 1742–1753, doi:10.1002/pip.2614.

[53] V. Sittinger, F. Ruske, W. Werner, C. Jacobs, B. Szyszka, D.J. Christie, High power pulsed magnetron sputtering of transparent conducting oxides, Thin Solid Films 516 (17) (2008) 5847–5859, doi:10.1016/j.tsf.2007.10.031.

[54] I. Petrov, F. Adibi, J.E. Greene, L. Hultman, J. Sundgren, Average energy deposited per atom: a universal parameter for describing ion-assisted film growth? Appl. Phys. Lett. 63 (1) (1993) 36–38, doi:10.1063/1.109742.

[55] L. Hultman, J. Sundgren, J.E. Greene, D.B. Bergstrom, I. Petrov, High-flux low-energy (~20 eV) N+2 ion irradiation during TiN deposition by reactive magnetron sputtering: Effects on microstructure and preferred orientation, J. Appl. Phys. 78 (9) (1995) 5395–5403, doi:10.1063/1.359720.

[56] K. Sarakinos, J. Alami, S. Konstantinidis, High power pulsed magnetron sputtering: a review on scientific and engineering state of the art, Surf. Coat. Technol. 204 (11) (2010) 1661–1684, doi:10.1016/j.surfcoat.2009.11.013.

[57] J. Narayan, B.C. Larson, Domain epitaxy: a unified paradigm for thin film growth, J. Appl. Phys. 93 (1) (2003) 278–285, doi:10.1063/1.1528301.

[58] S.S. Rao, J.T. Prater, F. Wu, S. Nori, D. Kumar, J. Narayan, Integration of epitaxial permalloy on Si(100) through domain matching epitaxy paradigm, Curr. Opin. Solid State Mater.Sci. 18 (1) (2014) 1–5, doi:10.1016/j.cossms.2013.07.004. Thin Film Heterostructures across the Misfit Scale and Impact on Nanotechnology

[59] J.A. Thornton, Influence of apparatus geometry and deposition conditions on the structure and topography of thick sputtered coatings, J. Vac. Sci. Technol. 11 (4) (1974) 666–670, doi:10.1116/1.1312732.

[60] P.B. Barna, M. Adamik, Fundamental structure forming phenomena of polycrystalline films and the structure zone models, Thin solid films 317 (1-2) (1998) 27–33.

[61] E. Kusano, Structure-zone modeling of sputter-deposited thin films: a brief review, Appl. Sci. Converg. Technol. 28 (6) (2019) 179–185, doi:10.5757/ASCT.2019.28.6.179.

[62] M. Ohring, Chapter 9 - film structure, in: M. Ohring (Ed.), Materials Science of Thin Films (Second Edition), 2nd ed., Academic Press, San Diego, 2002, pp. 495–558.

[63] G.H. Bishop, W.H. Hartt, G.A. Bruggeman, Grain boundary faceting of $\langle 10\bar{1}0 \rangle$ tilt boundaries in Zinc, Acta Metall. 19 (1) (1971) 37–47, doi:10.1016/0001-6160(71)90159-3.

[64] P.J. Goodhew, T.Y. Tan, R.W. Balluffi, Low energy planes for tilt grain boundaries in gold, Acta Metall. 26 (4) (1978) 557–567, doi:10.1016/0001-6160(78)90108-6.

[65] T. Muschik, W. Laub, U. Wolf, M.W. Finnis, W. Gust, Energetic and kinetic aspects of the faceting transformation of a Σ3 grain boundary in Cu, Acta Metall. Mater. 41 (7) (1993) 2163–2171, doi:10.1016/0956-7151(93)90386-7.

[66] A.M. Krzysztof Glowinski, Twist, tilt, and symmetric grain boundaries in hexagonal materials, J. Mater. Sci. 49 (2014) 3936–3942, doi:10.1007/s10853-013-7958-5.

[67] M.N. Kelly, K. Glowinski, N.T. Nuhfer, G.S. Rohrer, The five parameter grain boundary character distribution of $\alpha$-Ti determined from three-dimensional orientation data, Acta Mater. 111 (2016) 22–30, doi:10.1016/j.actamat.2016.03.029.

[68] E. Farabi, P.D. Hodgson, G.S. Rohrer, H. Beladi, Five-parameter intervariant boundary characterization of martensite in commercially pure titanium, Acta Mater. 154 (2018) 147–160, doi:10.1016/j.actamat.2018.05.023.

[69] A. Ostapovets, P. Molnr, P. LejÄek, Boundary plane distribution for Σ13 grain boundaries in magnesium, Mater. Lett. 137 (2014) 102–105, doi:10.1016/j.matlet.2014.08.152.

[70] G.S. Rohrer, B.S. El-Dasher, H.M. Miller, A.D. Rollett, D.M. Saylor, Distribution of grain boundary planes at coincident site lattice misorientations, MRS Proc. 819 (1) (2004) N7.2, doi:10.1557/PROC-819-N7.2.

[71] C.-S. Kim, Y. Hu, G.S. Rohrer, V. Randle, Five-parameter grain boundary distribution in grain boundary engineered brass, Scr. Mater. 52 (7) (2005) 633–637, doi:10.1016/j.scriptamat.2004.11.025.

[72] V. Randle, Y. Hu, G.S. Rohrer, C.S. Kim, Distribution of misorientations and grain boundary planes in grain boundary engineered brass, Mater. Sci. Technol. 21 (11) (2005) 1287–1292, doi:10.1179/174328405X66996.

[73] V. Randle, Relationship between coincidence site lattice, boundary plane indices, and boundary energy in nickel, Mater. Sci. Technol. 15 (3) (1999) 246–252, doi:10.1179/026708399101505806.

[74] T. Meiners, T. Frolov, R.E. Rudd, G. Dehm, C.H. Liebscher, Observations of grain-boundary phase transformations in an elemental metal, Nature 579 (7799) (2020) 375–378, doi:10.1038/s41586-020-2082-6.

[75] T. Frolov, D.L. Olmsted, M. Asta, Y. Mishin, Structural phase transformations in metallic grain boundaries, Nat. Commun. 4 (1) (2013) 1899, doi:10.1038/ncomms2919.

[76] P. Lejcek, Grain Boundary Segregation in Metals, vol. 136, Springer Science & Business Media, 2010.

[77] S. Hofmann, P. Lejcek, Solute segregation at grain boundaries, Interface Sci. 3 (4) (1996) 241–267, doi:10.1007/BF00194704.

[78] R. Kirchheim, Reducing grain boundary, dislocation line and vacancy formation energies by solute segregation. I. Theoretical background, Acta Mater. 55 (15) (2007) 5129–5138, doi:10.1016/j.actamat.2007.05.047.

[79] A.M. Donald, L.M. Brown, Grain boundary faceting in Cu-Bi alloys, Acta Metall. 27 (1) (1979) 59–66, doi:10.1016/0001-6160(79)90056-7.

[80] N.J. Peter, M.J. Duarte, C. Kirchlechner, C.H. Liebscher, G. Dehm, Faceting diagram for Ag segregation induced nanofaceting at an asymmetric Cu tilt grain boundary, Acta Mater. 214 (2021) 116960, doi:10.1016/j.actamat.2021.116960.

[81] I. Langmuir, The adsorption of gases on plane surfaces of glass, mica and platinum, J. Am. Chem. Soc. 40 (9) (1918) 1361–1403, doi:10.1021/ja02242a004.

[82] D. McLean, A. Maradudin, Grain boundaries in metals, Phys. Today 11 (7) (1958) 35.

[83] P. LejÄek, S. Hofmann, V. Paidar, Solute segregation and classification of [100] tilt grain boundaries in $\alpha$-iron: consequences for grain boundary engineering, Acta Mater. 51 (13) (2003) 3951–3963, doi:10.1016/S1359-6454(03)00219-2.

[84] P. Wynblatt, R.C. Ku, Surface energy and solute strain energy effects in surface segregation, Surf. Sci. 65 (2) (1977) 511–531.

[85] M.P. Seah, C. Lea, Surface segregation and its relation to grain boundary segregation, Philos. Mag. J. Theor. Exp. Appl. Phys. 31 (3) (1975) 627–645, doi:10.1080/14786437508226543.

[86] G. Bozzolo, J. Ferrante, J.R. Smith, Method for calculating alloy energetics, Phys. Rev. B 45 (1992) 493–496, doi:10.1103/PhysRevB.45.493.

[87] L. Ding, R. Hu, Y. Gu, D. Zhou, F. Chen, L. Zhou, H. Chang, Effect of Fe content on the as-cast microstructures of Ti-6Al-4V-xFe alloys, Metals 10 (8) (2020), doi:10.3390/met10080989.

[88] R.A. Outlaw, W.S. Lee, S.J. Hoekje, S.N. Sankaran, Sulfur segregation in titanium and selected titanium alloys, Appl. Surf. Sci. 81 (2) (1994) 143–150, doi:10.1016/0169-4332(94)00165-0.

[89] S. Suzuki, K. Abiko, H. Kimura, Phosphorus segregation related to the grain boundary structure in an Fe-P alloy, Scr. Metall. 15 (c) (1981) 1139–1143, doi:10.1016/0036-9748(81)90175-7.

[90] H. Fukushima, H.K. Birnbaum, High resolution saes and sims studies of grain boundary segregation of S and Cl in Ni, Scr. Metall. 16 (6) (1982) 753–757, doi:10.1016/0036-9748(82)90336-2.

[91] T. Walther, N. Daneu, A. Recnik, A new method to measure small amounts of solute atoms on planar defects and application to inversion domain boundaries in doped zinc oxide, Interface Sci. 12 (2) (2004) 267–275, doi:10.1023/B:INTS.0000028656.12913.8a.

[92] P. Doig, P. Flewitt, The detection of monolayer grain boundary segregations in steels using STEM-EDS X-ray microanalysis, Metall. Trans. A 13 (8) (1982) 1397–1403, doi:10.1007/BF02642877.

[93] D.A. Muller, S. Subramanian, P.E. Batson, J. Silcox, S.L. Sass, Structure, chemistry and bonding at grain boundaries in Ni3Al-I. The role of boron in ductilizing grain boundaries, Acta Mater. 44 (4) (1996) 1637–1645, doi:10.1016/1359-6454(95)00267-7.

[94] V.J. Keast, D.B. Williams, Quantitative compositional mapping of Bi segregation to grain boundaries in Cu, Acta Mater. 47 (15) (1999) 3999–4008, doi:10.1016/S1359-6454(99)00260-8.

[95] C.H. Liebscher, A. Stoffers, M. Alam, L. Lymperakis, O. Cojocaru-Mirédin, B. Gault, J. Neugebauer, G. Dehm, C. Scheu, D. Raabe, Strain-induced asymmetric line segregation at faceted Si grain boundaries, Phys. Rev. Lett. 121 (2018) 015702, doi:10.1103/PhysRevLett.121.015702.

[96] D. Raabe, M. Herbig, S. Sandlöbes, Y. Li, D. Tytko, M. Kuzmina, D. Ponge, P.-P. Choi, Grain boundary segregation engineering in metallic alloys: a pathway to the design of interfaces, Curr. Opin. Solid State Mater.Sci. 18 (4) (2014) 253–261, doi:10.1016/j.cossms.2014.06.002.

[97] K. Babinsky, J. Weidow, W. Knabl, A. Lorich, H. Leitner, S. Primig, Atom probe study of grain boundary segregation in technically pure molybdenum, Mater. Charact. 87 (2014) 95–103, doi:10.1016/j.matchar.2013.11.001.

[98] M. Herbig, Spatially correlated electron microscopy and atom probe tomography: Current possibilities and future perspectives, Scr. Mater. 148 (2018) 98–105, doi:10.1016/j.scriptamat.2017.03.017.

[99] N.J. Peter, C.H. Liebscher, C. Kirchlechner, G. Dehm, Beam-induced atomic migration at Ag-containing nanofacets at an asymmetric Cu grain boundary, J. Mater. Res. 32 (5) (2017) 968–982, doi:10.1557/jmr.2016.398.

[100] J.L. Murray, H.A. Wriedt, The O-Ti (Oxygen-Titanium) system, J. Phase Equilib. 8 (2) (1987) 148–165, doi:10.1007/BF02873201.

[101] N.S.H. Gunda, B. Puchala, A. Van der Ven, Resolving phase stability in the Ti-O binary with first-principles statistical mechanics methods, Phys. Rev. Mater. 2 (2018) 033604, doi:10.1103/PhysRevMaterials.2.033604.

[102] P. Maugis, K. Hoummada, A methodology for the measurement of the interfacial excess of solute at a grain boundary, Scr. Mater. 120 (2016) 90–93, doi:10.1016/j.scriptamat.2016.04.005.